NASA/TM-20210010291

Plug20 Test Report

James E. Bridges, Gary G. Podboy, and Mark P. Wernet
Glenn Research Center, Cleveland, Ohio

March 2021

NASA STI Program . . . in Profile

Since its founding, NASA has been dedicated to the advancement of aeronautics and space science. The NASA Scientific and Technical Information (STI) Program plays a key part in helping NASA maintain this important role.

The NASA STI Program operates under the auspices of the Agency Chief Information Officer. It collects, organizes, provides for archiving, and disseminates NASA's STI. The NASA STI Program provides access to the NASA Technical Report Server—Registered (NTRS Reg) and NASA Technical Report Server—Public (NTRS) thus providing one of the largest collections of aeronautical and space science STI in the world. Results are published in both non-NASA channels and by NASA in the NASA STI Report Series, which includes the following report types:

- TECHNICAL PUBLICATION. Reports of completed research or a major significant phase of research that present the results of NASA programs and include extensive data or theoretical analysis. Includes compilations of significant scientific and technical data and information deemed to be of continuing reference value. NASA counter-part of peer-reviewed formal professional papers, but has less stringent limitations on manuscript length and extent of graphic presentations.

- TECHNICAL MEMORANDUM. Scientific and technical findings that are preliminary or of specialized interest, e.g., "quick-release" reports, working papers, and bibliographies that contain minimal annotation. Does not contain extensive analysis.

- CONTRACTOR REPORT. Scientific and technical findings by NASA-sponsored contractors and grantees.

- CONFERENCE PUBLICATION. Collected papers from scientific and technical conferences, symposia, seminars, or other meetings sponsored or co-sponsored by NASA.

- SPECIAL PUBLICATION. Scientific, technical, or historical information from NASA programs, projects, and missions, often concerned with subjects having substantial public interest.

- TECHNICAL TRANSLATION. English-language translations of foreign scientific and technical material pertinent to NASA's mission.

For more information about the NASA STI program, see the following:

- Access the NASA STI program home page at http://www.sti.nasa.gov

- E-mail your question to help@sti.nasa.gov

- Fax your question to the NASA STI Information Desk at 757-864-6500

- Telephone the NASA STI Information Desk at 757-864-9658

- Write to:
  NASA STI Program
  Mail Stop 148
  NASA Langley Research Center
  Hampton, VA 23681-2199

NASA/TM-20210010291

Plug20 Test Report

James E. Bridges, Gary G. Podboy, and Mark P. Wernet
Glenn Research Center, Cleveland, Ohio

National Aeronautics and
Space Administration

Glenn Research Center
Cleveland, Ohio 44135

March 2021

Acknowledgments

The Plug20 test was supported by the NASA Commercial Supersonic Technology project, under the Advanced Air Vehicle Program. The staff of the Aero-Acoustic Propulsion Laboratory did their usual supremely professional job in the face of the oncoming epidemic and quarantine, making the most of the few test days available. The thorough review of the manuscript by Khairul Zaman is appreciated.

This work was sponsored by the Advanced Air Vehicle Program at the NASA Glenn Research Center

Level of Review: This material has been technically reviewed by technical management.

Available from

NASA STI Program
Mail Stop 148
NASA Langley Research Center
Hampton, VA 23681-2199

National Technical Information Service
5285 Port Royal Road
Springfield, VA 22161
703-605-6000

This report is available in electronic form at http://www.sti.nasa.gov/ and http://ntrs.nasa.gov/

Plug20 Test Report

James E. Bridges, Gary G. Podboy, and Mark P. Wernet
National Aeronautics and Space Administration
Glenn Research Center
Cleveland, Ohio 44135

Abstract

This report documents a test of aircraft exhaust nozzle designs applicable to commercial supersonic aircraft as envisioned in the 2025 to 2035 time frame. The test is primarily intended to provide data about the noise such aircraft would produce during landing and takeoff (LTO) operation, specifically the jet noise component of this noise. The tests were conducted at the NASA Glenn Research Centers Aero-Acoustic Propulsion Laboratory (AAPL) in March 2020. The tests used the High-Flow Jet Exit Rig in the Nozzle Acoustic Test Rig (NATR) which simulates the flow from a dual-stream turbofan engine in a flight stream. Seven exhaust configurations were tested with various combinations of internal mixer and external plug, and covered engine cycles having nozzle pressures from 1.5 to 2.3 at a flight speed of Mach 0.3. A few unheated flow conditions were also tested to tie results to other baseline test results.

Data acquired and included in this report are (1) far-field acoustic spectra, (2) phased array measurements of noise source distributions, and (3) background-oriented schlieren of the flow near the nozzles. These data, along with the nozzle geometry in Computer aided drawing (CAD) format, are given as Appendices and are available online.

Nomenclature and Abbreviations

AAPL	Aero-Acoustic Propulsion Laboratory
B&K	Bruel & Kjaer, microphone manufacturer
BBSN	Broadband shock noise
BOS	background-oriented schlieren
BPR	Bypass Ratio, mass of bypass/mass of core
CAD	Computer aided drawing
Cd	Discharge coefficient, measured mass flow/ideal mass flow
CFD	Computational Fluid Dynamics
DADS	Digital Acoustic Data System
Djet	jet diameter
GPU	Graphics Processing Unit
HFJER	High-Flow Jet Exit Rig
Ma	Mach number, ideally expanded, based on ambient speed of sound.
Mfj	Mach number of freejet (flight stream)
M, Mid	Mach number, ideally expanded, based on speed of sound in flowing gas

NATR	Nozzle Acoustic Test Rig
NPR	Nozzle pressure ratio, jet total pressure/ambient pressure
NTR	Nozzle temperature ratio, jet total temperature/ambient temperature
RANS	Reynolds-Averaged Navier-Stokes
SHJAR	Small Hot Jet Acoustic Rig
St	Strouhal number, = frequency [Hz]*Djet [ft]/Ujet [ft/s]
TKE	Turbulent kinetic energy
Ujet	Jet exit velocity, fully expanded
W	Mass flow, ideal based on nozzle geometry, lbm/sec
Wact	Mass flow, measured, lbm/sec

Subscripts:

B	bypass
C	core
N	nozzle (total)

1.0 Introduction

The engine jet plume is the dominant noise source of commercial supersonic aircraft proposed for entry into service in 2025 to 2035. Due to cruise performance, nozzles with internal mixing of core and bypass streams with large external plugs are being considered for these aircraft. Empirical noise prediction methods generally do not account for the presence of internal mixers or an external plug and have no ability to account for differences in internal mixer design. Previously, tests have been made of exhaust systems with internal mixers and published results (Refs. 1 to 3) show the difficulty in creating such models. More advanced methods, such as Reynolds-Averaged Navier-Stokes (RANS)-based Computational Fluid Dynamics (CFD) with acoustic analogy noise codes, may be adequate but they do not account for the presence of the plug and cannot predict the propagation of noise generated internal to the nozzle. Furthermore, external plug nozzles have shocks from the curvature of the flow over the crown of the plug and no method exists to predict this noise source. It is also anticipated that the close proximity of the nozzle shear layer with an elongated plug may change the coupling of the turbulence with the acoustic field. Indeed, some work (Ref. 4) has shown that a properly shaped plug may even produce noise reduction.

As data for plug nozzles such as these are scarce, a baseline test is needed to determine the accuracy of the various noise prediction methods. This test will also determine the sensitivity of the noise to internal mixer design, plug length and shape. The noise of external plug nozzles was compared to equivalent internal plug nozzle with the same mixers to separate effects of the design features. A series of external plug nozzles, and corresponding internal plug nozzles for comparison, have been designed and fabricated. The designs were picked based on RANS flow simulations to provide meaningful changes in the flow with the changes in design parameters. The configuration nomenclature is described in the Model Hardware section below, but by way of motivation, flow features specific to external plug nozzles are discussed first.

Figure 1 shows the turbulent kinetic energy (TKE) of the reference internal-plug nozzle with two different mixers. Figure 2 and Figure 3 show the TKE of an external-plug nozzle with different duct lengths between the mixer and the nozzle exit. Note that the color scales are the same for all figures except Figure 1 which required a much larger span. The effect of plug length is shown in Figure 4. Note that the TKE is not affected greatly by the plug length, but it is anticipated that the additional length will change how the TKE is converted into sound. Figure 5 shows the mean axial velocity near the exit of the internal-plug nozzle with the two different mixers. Figure 6 illustrates the slight change in the plug shock with a subtle change in plug shape (*p2068* vs. *p2069*) and with a lengthening of the plug (*p2079*). The differences in the TKE of these variations, all of whom have the same engine flow conditions, indicates that they should have differences in their noise as well.

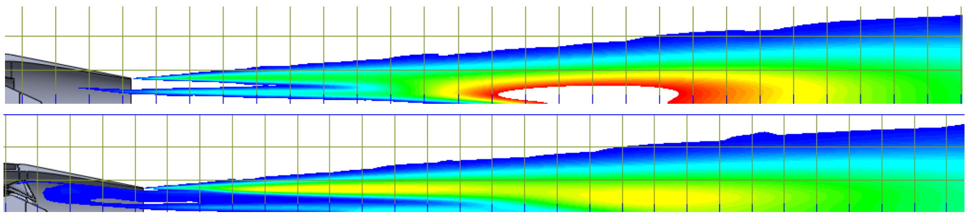

122A
Mixer *m0*
internal plug

122A
Mixer *m5*
internal plug

Figure 1.—TKE of Internal plug nozzles with internal mixers *m0* and *m5*. TKE scale is from 100 to 5000 J/kg.

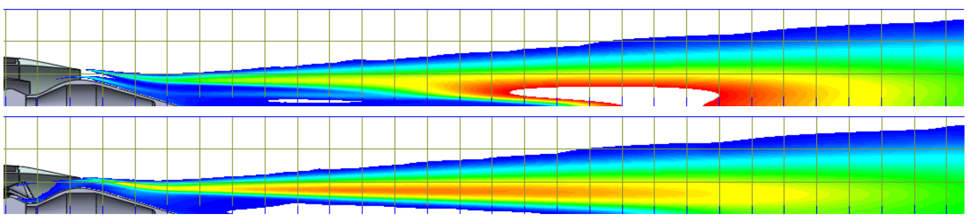

122DS
Mixer *m0*
p2069 plug

122DS
Mixer *m5*
p2069 plug

Figure 2.—TKE of Short-duct, external plug nozzles with internal mixers *m0* and *m5*. TKE scale is from 100 to 3500 J/kg.

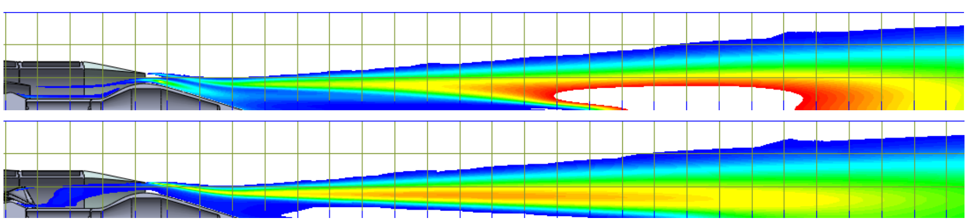

122DL
Mixer *m0*
p2069 plug

122DL
Mixer *m5*
p2069 plug

Figure 3.—TKE of long-duct, external plug nozzles with internal mixers *m0* and *m5*. TKE scale is from 100 to 3500 J/kg.

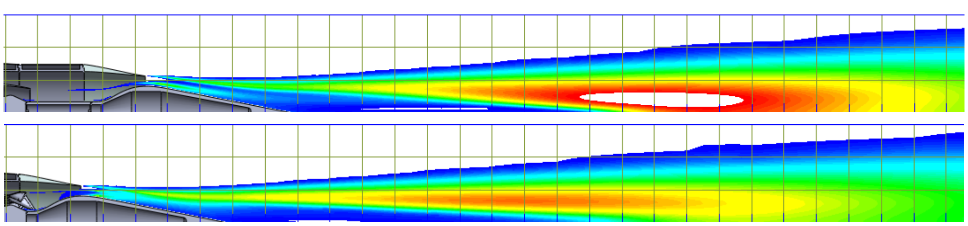

122DL
Mixer *m0*
p2079 plug

122DS
Mixer *m5*
p2079 plug

Figure 4.—TKE of external plug nozzles with long external plug and internal mixers *m0* and *m5*. TKE scale is from 100 to 3500 J/kg.

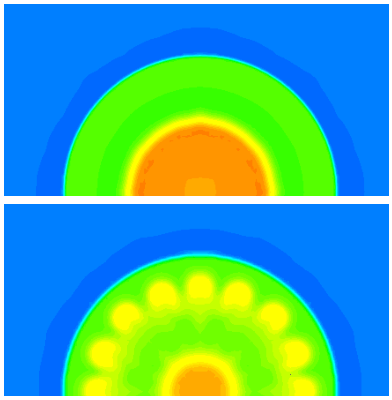

122A
Mixer *m0*
Internal plug

122A
Mixer *m5*
Internal plug

Figure 5.—Velocity cross-section at nozzle exit, internal plug nozzles with internal mixers *m0* and *m5*. Velocity scale is from 0 to 650 m/s.

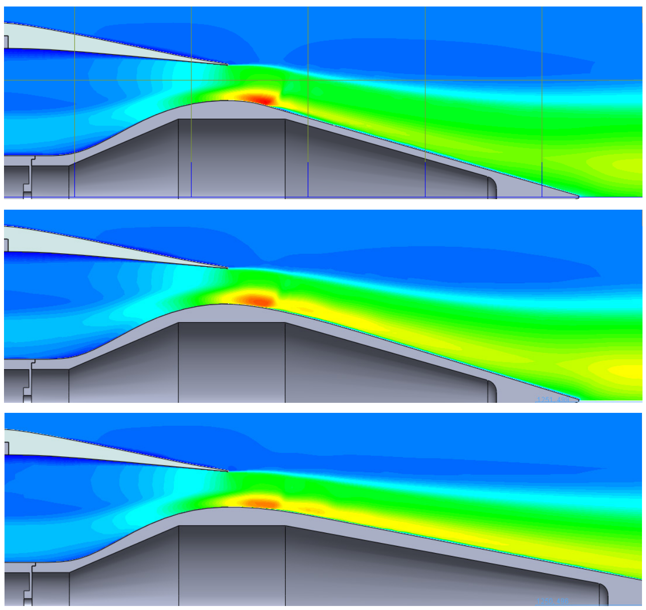

122DL
Mixer *m0*
p2068 plug

122DL
Mixer *m0*
p2069 plug

122DL
Mixer *m0*
p2079 plug

Figure 6.—Shocks on plugs *p2068*, *p2069*, and *p2079* with mixer *m0* on long-duct nozzle as seen in velocity on a streamwise plane through jet centerline. Velocity scale is from 0 to 650 m/s.

The nozzle configurations shown in the above Figures were selected from a larger set of geometries studied numerically and were tested in a test entry at NASA Glenn. This test report will document the configurations and flow conditions tested, the instrumentation systems used, and give a cursory analysis of the results to address how much of the test objectives were met.

2.0 Facility

The test was conducted in the NASA Glenn Research Center Aero-Acoustic Propulsion Laboratory (AAPL). The AAPL is a 65-ft radius anechoic geodesic hemispherical dome. Acoustic wedges cover the walls of the dome and approximately half of the floor area. AAPL is acoustically clean for all acoustic test runs, with acoustic wedges on the front and microphone sides of all rigs and on the floor of the facility. No untreated objects were within 15 ft of the jet nozzle and these were shielded from the microphones to avoid reflections. For this test additional instrumentation was present, and the lack of reflection by its presence is carefully documented in sections below.

The test articles were placed on a jet engine simulator, itself centered in the Nozzle Aeroacoustic Test Rig (NATR) contained in the AAPL. The NATR provides the flight stream for the jet rig. The NATR ductwork is acoustically lined on both the inside and outside and consisted of an annular ejector system connected to a plenum followed by the transition section which is a long-radius, low-beta venturi nozzle. This flow exhausts through a 53-in. diameter nozzle to form a free jet to simulate the effects of flight on the test article. The centerline of the free jet is 10 ft above the floor. This arrangement will produce Mach numbers in the free jet up to 0.35. An acoustically treated wall separates the NATR from the section of the building which did not have acoustic treatment on the floor, preventing unwanted reflections from the both the untreated floor area and adjacent test equipment.

A turbofan engine simulator, the High Flow Jet Exit Rig (HFJER), is located at the downstream end of the NATR. Compressed air from centralized compressors was delivered to the test article through a system of manifolds, heaters, flow measuring venturis, control valves, and flow conditioners. All air streams were preheated using a mixed flow heat exchanger before being split into two streams, independently metered and pressure-controlled, and directed to co-annular settling chambers in the rig. The innermost air stream was further heated using a natural gas combustor up to 1350 °F. The combined mass flow of the two streams was under 30 lbm/sec.

The rig was instrumented to record total temperature, total pressure, and static pressure at a charging station on all streams. In addition, mass flowrates were recorded using venturi meters. Ambient conditions were recorded simultaneously with the acoustic and flow measurements. Relative humidity and temperature were recorded both at 10 ft above the floor near the NATR and at the top-most region of the overhead microphone array, located roughly 60 ft above the floor. The overhead temperature was used in correcting the acoustic data, but the measurements at 10 and 60 ft were checked to be sure there were negligible temperature gradients that would complicate the corrections. Ambient pressure was recorded in a sheltered location within the dome.

Figure 7 shows a fish-eye view of the test venue, with the rigs centered in the anechoic dome.

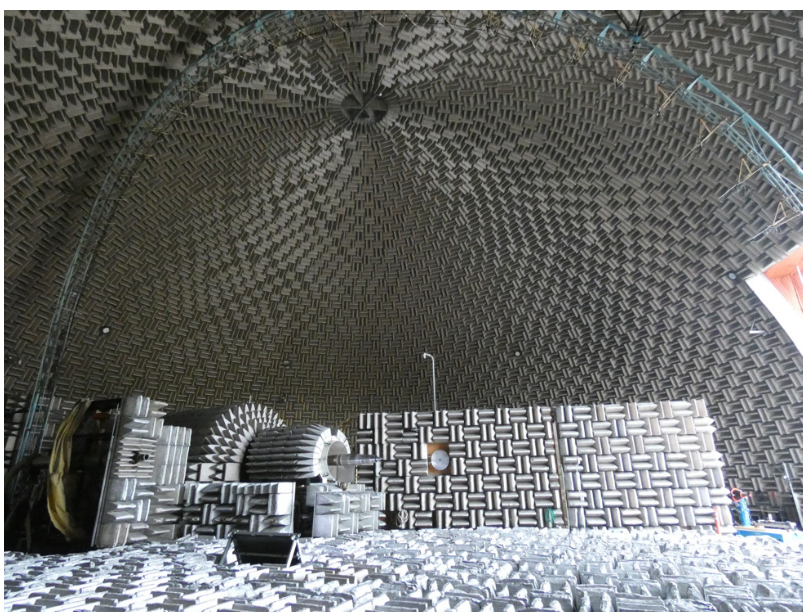

Figure 7.—View of test venue, with HFJER located at the exit of NATR, itself located within the anechoically treated AAPL.

The research instrumentation consisted of the far-field microphone array, a background-oriented schlieren (BOS) system, and a 48-microphone phased array. The BOS and phased array measurement systems were operated simultaneously. The overhead microphone array required the entire dome test area to be covered in acoustic wedges. The phased array and BOS systems required special mounting and were configured to remove their reflection from reaching the far-field microphones.

3.0 Model Hardware

Model configurations are comprised of a combination of plug, internal mixer, and nozzle. Configurations are first grouped as *internal* versus *external* plug. Figure 8 illustrates the difference in these configurations.

The internal plug configuration uses nozzle *122A*, and there is a choice of between two interchangeable mixers (*m0*, *m5*). The external plug configurations use nozzle *122D*, and there is a choice of three plugs (*p2068*, *p2069*, *p2079*) that can be used interchangeably with the two mixers. In addition, for the external plug configurations, spacers in the plug stem and nozzle duct allow a 7.9 in. (0.2 m) extension between the mixer and the nozzle exit plane. Thus the external nozzle designation is *122DS* (short, without extensions) and *122DL* (long, with extensions). A menu of components is given in Table 1. Note that nozzle *122DL* is nozzle *122DS* plus the duct extension and was only used with the plug extension for an external plug configuration. Figure 9 to Figure 11 give a visual reference of the various components which make up the different configurations. Figure 12 compares the radial profiles of plugs *p2068* and *p2069*, which differ only in the transition from the rounded crown to the conic taper. Finally, Figure 13 and Figure 14 give cross-sections of the internal plug and external plug nozzles respectively. These two figures show critical dimensions of the assemblies.

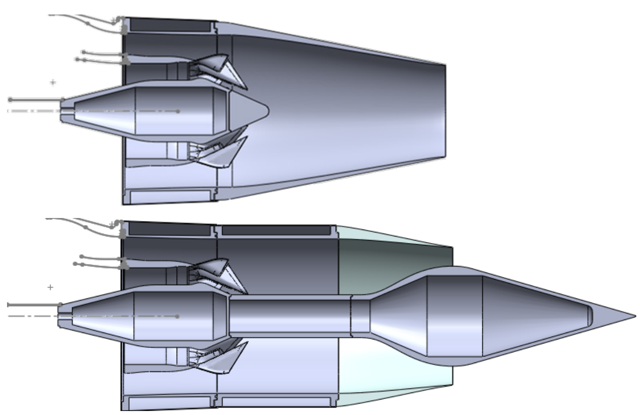

Figure 8.—Internal plug vs. external plug configurations.

TABLE 1.—INTERCHANGEABLE COMPONENTS WHICH COMPRISE EXHAUST SYSTEM CONFIGURATIONS

Nozzle	Mixer	Plug
122A	*m0*	*internal*
122DS	*m5*	*p2068*
122DL	----	*p2069*
--------	----	*p2079*

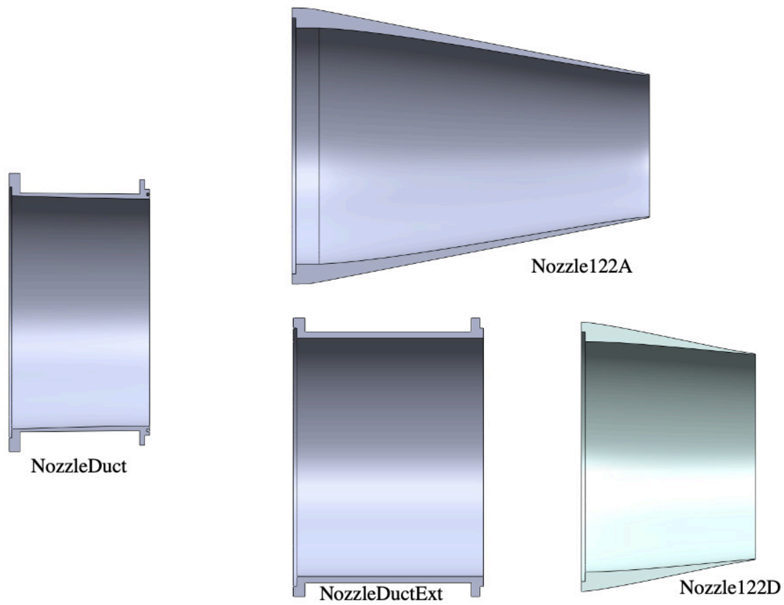

Figure 9.—Nozzle duct components: NozzleDuct (common to all configurations), Nozzle *122A* (internal plug configuration), Nozzle *122D* (external plug configurations), NozzleDuctExt (long duct configurations).

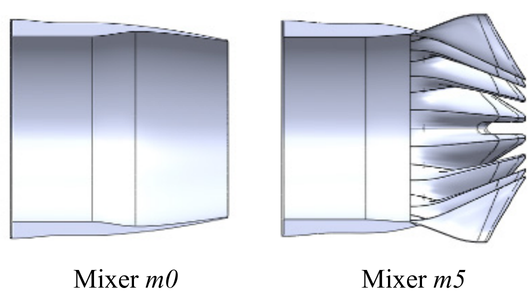

Figure 10.—Interchangeable mixers for test.

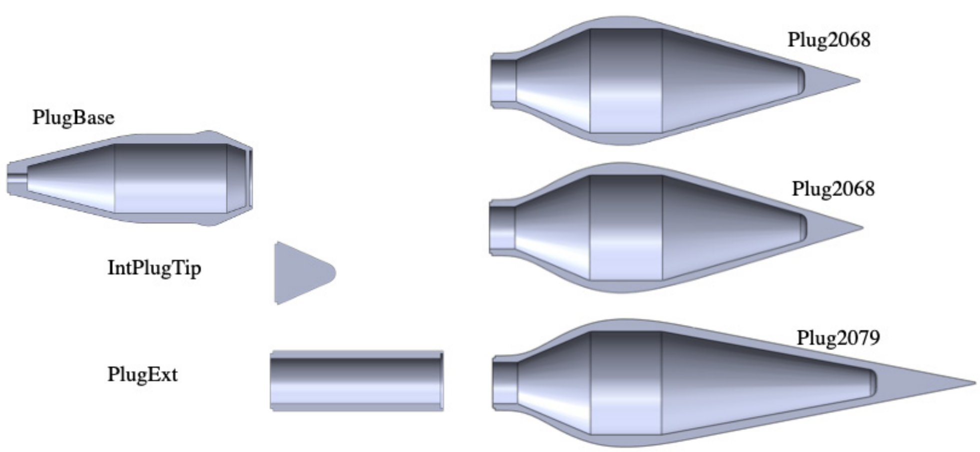

Figure 11.—Plug components: PlugBase (common), IntPlugTip for internal plug configuration, short plug with shock (*p2068*), short plug without shock (*p2069*), long plug (*p2079*), PlugExtension for long duct configuration.

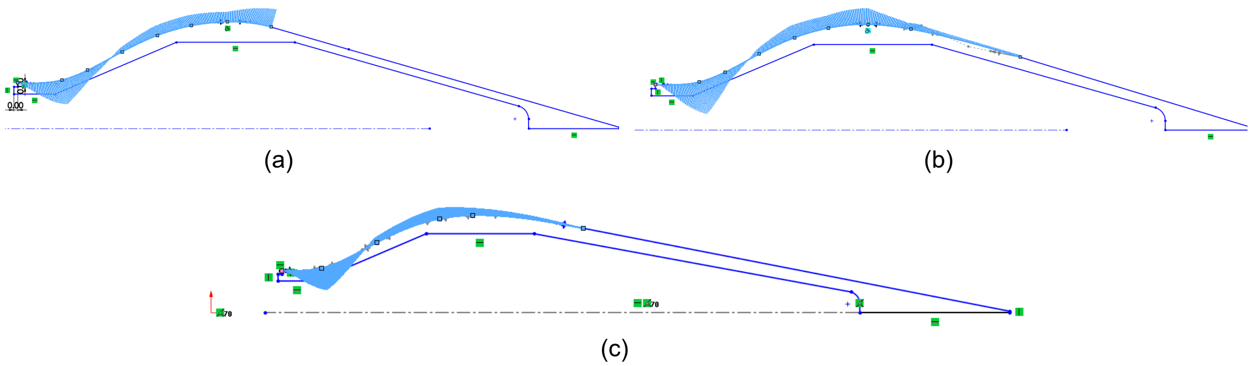

Figure 12.—Profiles of plug designs (a) *p2068*, (b) *p2069*, and (c) *p2079*. Note curvature combs in blue showing abrupt change in curvature in *p2068* and continuous transition of curvature on *p2069* and *p2079*.

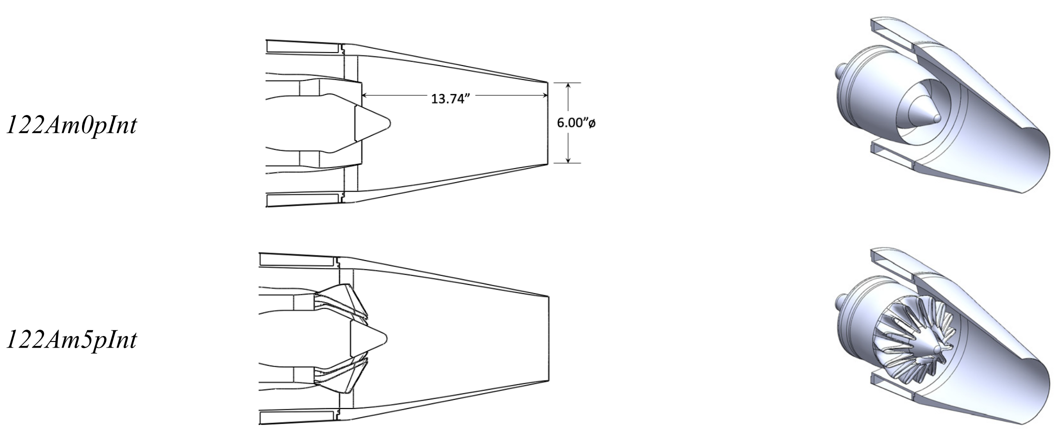

Figure 13.—Internal plug configurations tested, in profile and in cutaway views.

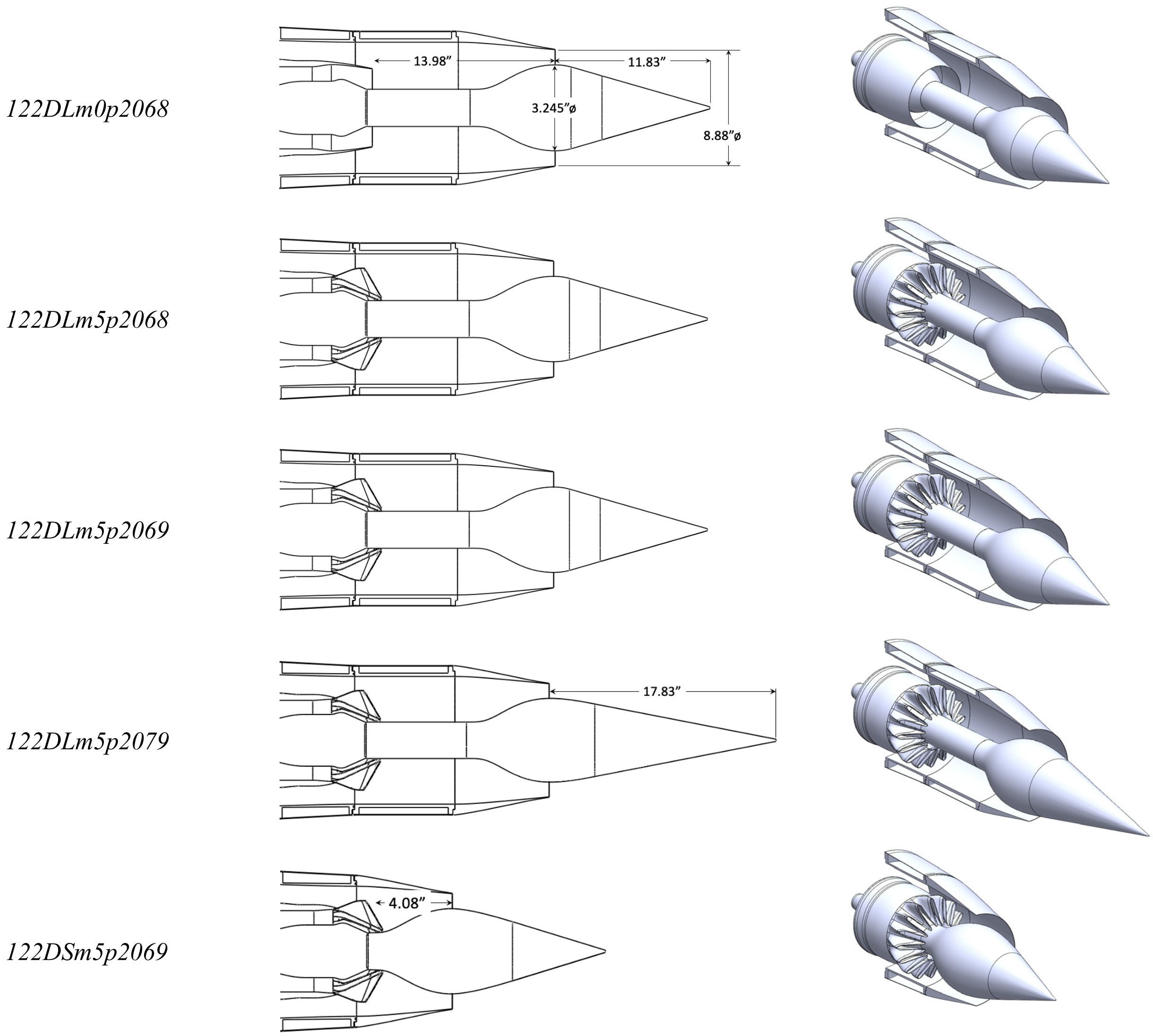

Figure 14.—External plug configurations tested, in profile and in cutaway views.

TABLE 2.—FLOW DATA FOR UNHEATED, PRESSURE MATCHED FLOWS, GIVING ESTIMATES OF FLOW AREAS FOR TESTED CONFIGURATIONS
[C-Core, B-Bypass, N-Nozzle (Total)]

Configuration	$Wact_C$, lbm/s	$Wact_B$, lbm/s	$Wact_N$, lbm/s	BPR	A_C8eq, in.^{2}	A_B8eq, in.^{2}	A_N8eq, in.^{2}	C_d re 6 in. ø
122Am0pInt	5.59	12.13	17.7	2.17	8.87	19.23	28.10	0.993
122Am5pInt	5.12	12.48	17.6	2.44	8.15	19.92	28.07	0.992
122DLm0p2068	5.14	12.87	18.0	2.50	8.19	20.47	28.66	1.013
122DLm5p2068	4.60	12.90	17.5	2.80	7.65	20.90	28.54	1.009
122DLm5p2069	4.47	13.02	17.5	2.91	7.38	21.15	28.54	1.009
122DLm5p2079	4.67	13.25	17.9	2.83	7.44	21.05	28.49	1.007
122DSm5p2069	4.51	13.18	17.7	2.93	7.42	21.13	28.55	1.009

As originally designed, the axisymmetric splitter and lobed mixer were intended to have the same flow areas. In later review it was found that the axisymmetric splitter *m0* had a larger flow area than the *m5* mixer on the same plug, and that all the mixers had greater effective flow areas when installed with the external plug. These variations in effective flow area meant that the configurations did not have the same bypass ratios. The weight flows from an unheated matched flow condition (setpoint 7; see below) gave a measure of relative flow areas (Table 2). Note that when configurations were the second configuration of a test day the rig retained some residual heat. Thus, the flow was not completely unheated, but had core total temperature ratios just under 1.1. The discharge coefficient is computed from the total measured mass flow ($Wact_N$) divided by ideal mass flow for the measured flow conditions.

From the data in the table, it appears that (1) the external plug nozzle had an area 1.5 percent greater than the internal plug nozzle, (2) the external plug nozzle had an area ratio (bypass/core) 16 percent greater than the internal plug nozzle, (3) the *m5* lobed mixer produced an area ratio (bypass/core) 13 percent greater than the *m0* mixer. The end result is that some accommodation will have to be made when comparing configurations as they will not be operating at the same mass flow bypass ratios. The core and bypass mass flow measurements, made with unchoked venturis, are accurate to roughly 0.05 and 0.15 lbm/s, respectively.

4.0 Flow Conditions

The flow conditions tested were meant to mimic a potential two-stream engine for commercial supersonic aircraft. Specifically, they followed a generic engine cycle for an engine, with an extension in NPR and a fixed temperature ratio. This matrix is given in Table 3. The weight flows are from original design areas; actual weight flows vary (see Table 4).

The engine cycle matrix is given in visual form in Figure 15. The pressure ratios and temperature ratios for the core and bypass streams are shown in the solid circles. The corresponding weight flows are given by the open X, referenced to the right vertical axis.

One of the most significant acoustic attributes being explored is the broadband shock noise (BBSN). External plugs have external shocks where the flow curves over the plug near the nozzle exit. This shock system is relatively insensitive to temperature and exists well below critical pressure ratio. Noise prediction models for this BBSN have not been created and the phenomena needs to be better documented. Also, two of the plugs were designed to have different shock strengths for the same basic parameters, an unheated BBSN matrix was defined (Table 5) to allow comparisons with classic measurements of BBSN. This matrix was run before heating the rig for the day but was only run on configuration *122Am0pInt* due to time constraints.

The setpoints were held constant to within a cumulative 0.5 percent error.

TABLE 3.—ENGINE CYCLE MATRIX

Setpoint	NPR	NTRc	NTRb	Mfj	Wc, lbm/s	Wb, lbm/s	Uj, m/s
1233	2.3	3.25	1.25	0.3	3.44	14.08	629
1223	2.2	3.25	1.25	0.3	3.29	13.47	614
1213	2.1	3.25	1.25	0.3	3.14	12.86	597
1203	2.0	3.25	1.20	0.3	2.99	12.50	579
1193	1.9	3.10	1.20	0.3	2.91	11.87	546
1183	1.8	2.90	1.20	0.3	2.63	11.53	507
1173	1.7	2.75	1.20	0.3	2.54	10.82	470
1162	1.6	2.60	1.15	0.25	2.43	10.27	432
1152	1.5	2.40	1.15	0.25	0.99	9.41	387

TABLE 4.—SAMPLE ACTUAL WEIGHT FLOWS GIVING BPR FOR CYCLE POINT 1203 (DEFINED BELOW)
[C-Core, B-Bypass, N-Nozzle (Total)]

Configuration	WactC, lbm/s	WactB, lbm/s	WactN, lbm/s	BPR
122Am0pInt	3.32	11.79	15.1	3.56
122Am5pInt	3.02	11.89	14.9	3.93
122DLm0p2068	3.00	12.31	15.3	4.10
122DLm5p2068	2.80	12.42	15.2	4.44
122DLm5p2069	2.78	12.26	15.0	4.40
122DLm5p2079	2.76	12.54	15.3	4.54
122DSm5p2069	2.80	12.57	15.4	4.49

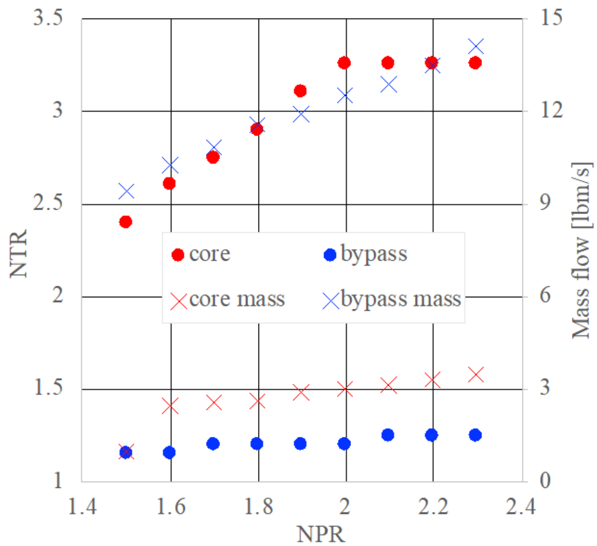

Figure 15.—Engine cycle matrix, total temperature ratio (NTR) vs. pressure ratio (NPR) for core and bypass streams. Expected mass flows given on right-hand axis.

TABLE 5.—BBSN MATRIX—SINGLE-STREAM, UNHEATED FLOWS

Setpoint	NPR	NTR	Mid
3	1.197	1	0.51
5	1.435	1	0.73
7	1.856	1	0.98
401	1.893	1	1.00
402	1.915	1	1.01
403	1.938	1	1.02
404	1.984	1	1.04
405	2.033	1	1.06
406	2.083	1	1.08
407	2.135	1	1.10

5.0 Instrumentation

5.1 Far-field Acoustics (FF24)

A 24-microphone arc array (24FF) was used for far-field spectral directivity. The array is the standard overhead array used for NATR testing with 1/4 in. microphones and preamps mounted on articulated microphone holders, shown in Figure 16. The microphones were adjusted to point at the internal nozzle exit.

Bruel & Kjaer™ (Hottinger Brüel & Kjær A/S) B&K 4939 microphones were used with the Nexus power supply/signal conditioner. Data were acquired on a DataMAX acquisition computer and transferred to a Linux computer for processing with Escort data. LTV personnel were responsible for operation of far-field acoustic instrumentation with assistance from the AAPL technicians in setup and calibration. End-to-end *insitu* calibrations of the microphones were performed at the beginning of the test and before the last day of testing.

5.2 Real-Time Background Oriented Schleiren (BOS)

Background Oriented Schlieren (BOS) is a widely used technique for measuring density gradients in fluid flows of interest. The attraction of BOS is the simplicity in the setup and data reduction. In this work two innovations to the BOS technique were employed. First, a GPU-based computer was used to acquire and process the BOS image data in real-time, providing a live display of the density gradients in the flow (Refs. 5 and 6). Secondly, an innovative approach for generating the background speckle patterns was employed. The speckle patterns required for the BOS measurement were displayed on a high definition 4K resolution computer monitor. Use of the 4K monitor to display the speckle patterns has three distinct advantages: (1) the speckle patterns can be generated on the computer and displayed directly on the monitor without having to physically construct the speckle pattern; (2) the scale of the speckle pattern can be readily changed to optimize the BOS system performance; and (3) the speckle pattern is self-illuminating, which greatly simplifies implementing the technique in confined environments, or where illumination of a static speckle pattern may be difficult or problematic. In the case of the Plug20 test, the self-illuminated background eliminated the need for additional illumination sources which could have increased the acoustic degradation of the facility. A 2.4x2K pixel, GigE interface camera was used to image the speckle pattern displayed on an 86 in. diagonal 4K resolution monitor. A binary dot speckle pattern was used, in order to obtain a high contrast background pattern over the long imaging distance from the camera to the monitor (27 ft). The processed density gradient maps were acquired, processed and displayed by a dedicated computer located in the control room at a 10 Hz frame rate.

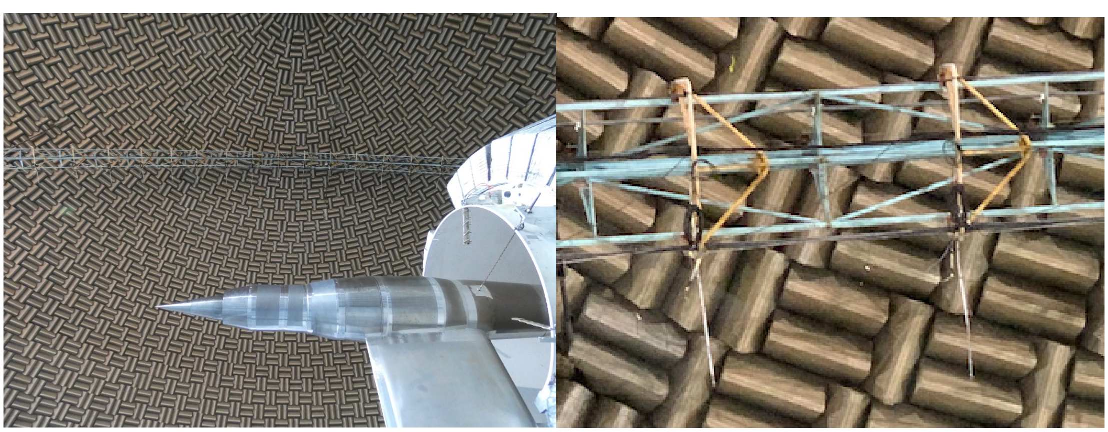

Figure 16.—Overhead array above nozzle model. Each microphone was mounted on a sting oriented at 45° to the microphone axis and attached to each golden carriage on blue track.

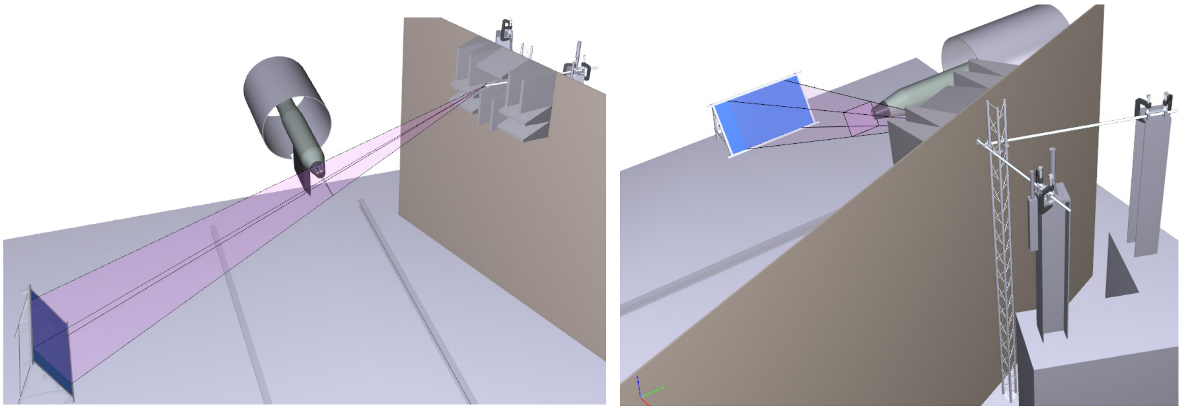

Figure 17.—CAD rendering of the Real-Time-BOS installation illustrating (a) the camera mounting location in the wedge wall and its field of view of the BOS monitor, (b) backside view of the camera installation and support on the vertical truss structure.

Typically, flow diagnostics are not possible during acoustic testing without the diagnostic system causing undesirable acoustic reflections. Traditional Schlieren is difficult to implement in acoustic facilities due to the high noise levels and the optical system's sensitivity to vibrations. Real-Time-BOS enables real-time visualization of the shocks in the flow, without all of the traditional Schlieren sensitivities to vibration and requisite large mirrors and supporting hardware which could cause acoustic reflections. For the Plug20 test, measurements of the flow field information during the acoustic measurement portion of the test was attempted for the first time by specifically designing the Real-Time-BOS system into the NATR environment to minimize the acoustic signature. Figure 17(a) shows a CAD rendering of the Real-Time-BOS system installation in the AAPL. The BOS camera truss mount is shown in Figure 17(b). For the Plug20 test, the speckle background field was displayed on an 86 in. diagonal monitor located on the floor of the facility within the wedges. The 4K monitor was mounted perpendicular to the plane of the overhead microphone array, at a 25° angle from the vertical. The small (1x1x1 in.) GigE camera (Figure 18) used to acquire the BOS image data was mounted off a vertical tower on the backside of the wedge wall (Figure 17(b)). The camera mount was not coupled to the wedge wall to avoid any motion/vibrations of the camera from the wedge wall during the test.

Once the BOS monitor was deployed its location could not be easily changed. The test articles, however, had different lengths, making the choice of the field-of-view critical. The primary objective was to record shocks on the external plugs and in the initial flow region of the internal plug configurations. Figure 19 shows a rendering of the field of view superimposed over both short- and long-duct external plug configurations. Note (from comparison of Figure 13 and Figure 14) that the internal plug nozzle had the same exit location as the nozzle of the long-duct external plug nozzle.

A sample raw image from the Real-Time-BOS system is shown in Figure 20, where the binary dot background can be seen along with the model. The BOS monitor is clearly embedded amongst the wedges. Figure 21 shows a sample set of processed BOS data overlaid on a raw BOS image.

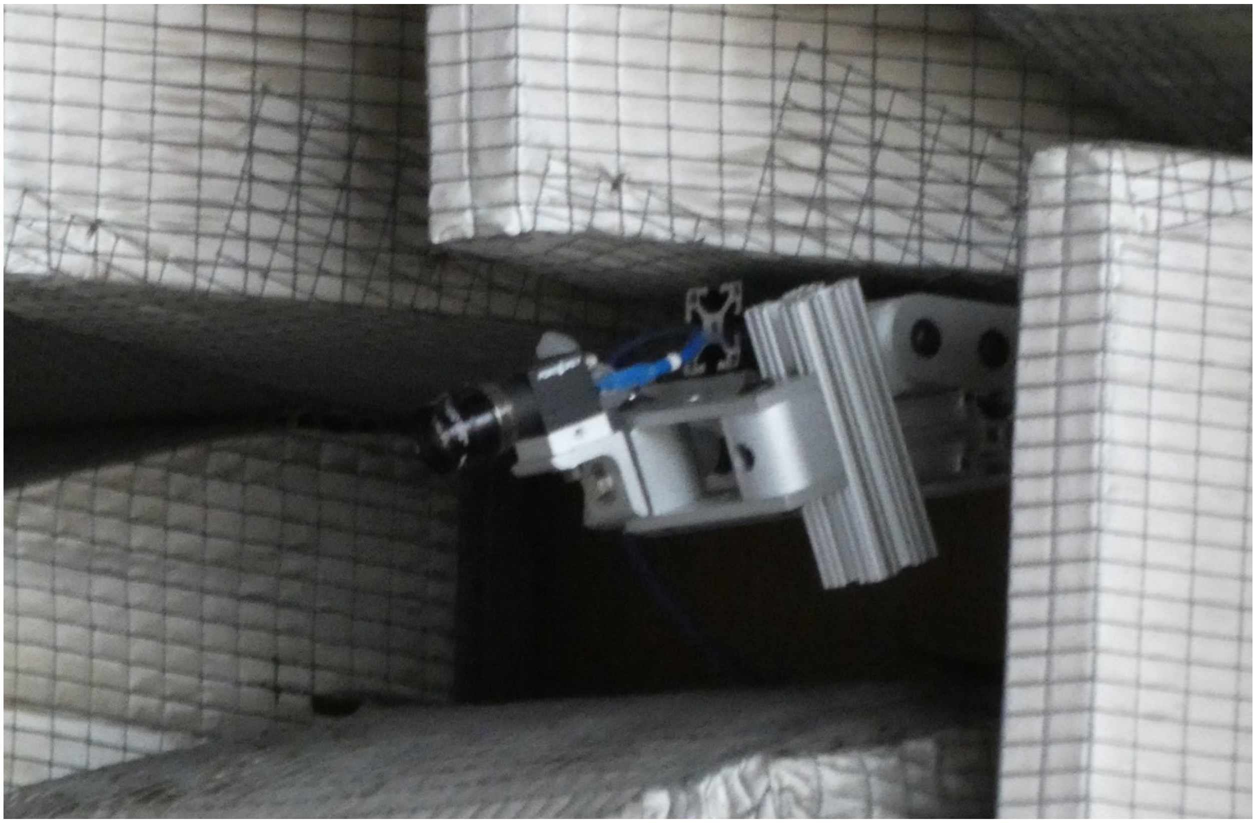

Figure 18.—Real-Time-BOS camera embedded in the NATR wedge wall, mounted through wall to hard supports.

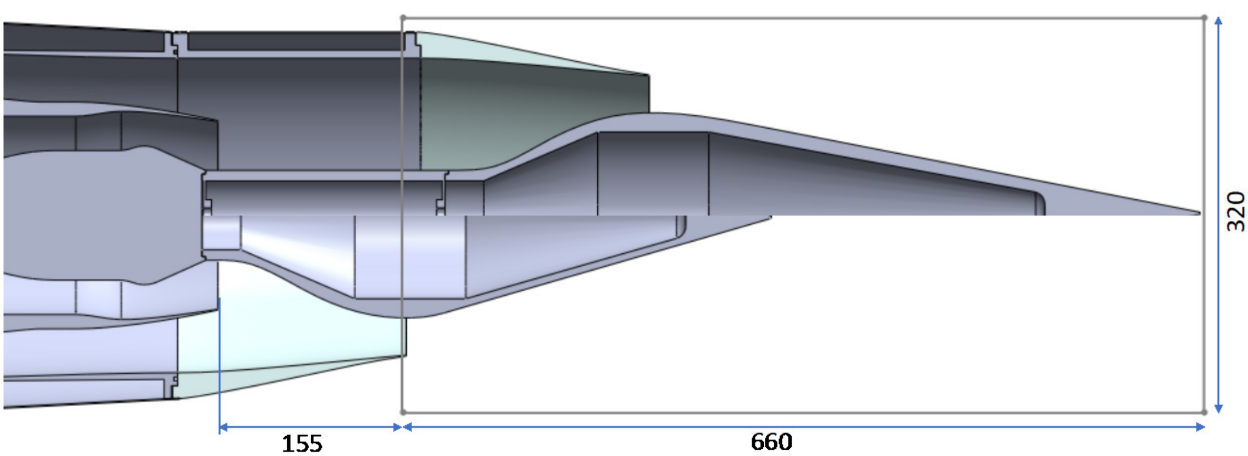

Figure 19.—Optimal field of view for BOS to cover nozzle exit to plug for all configurations. Upper half is long-duct, long-plug configuration, lower half is short-duct, nominal plug configuration.

Figure 20.—Raw BOS image showing background speckle pattern. The model is 20 ft away from the background.

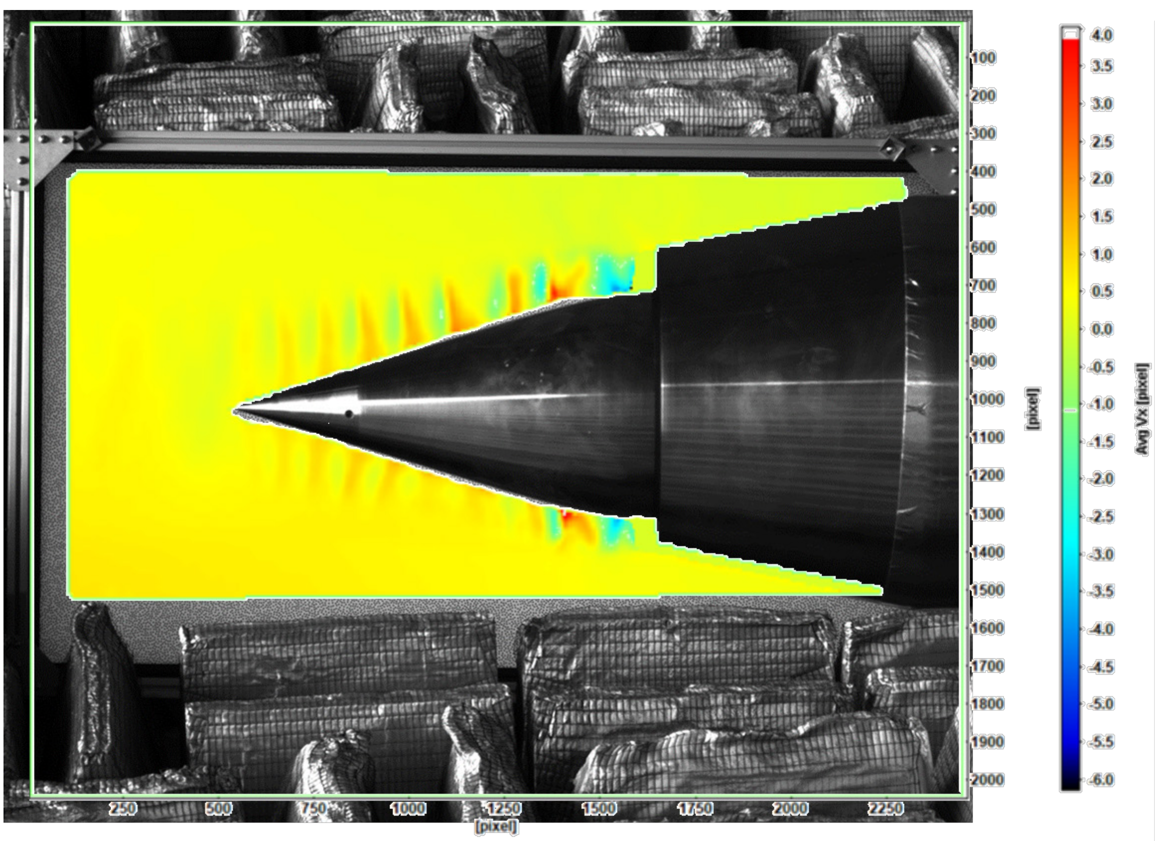

Figure 21.—Processed BOS data (Setpoint 1223 on *122DLm5p2069*) overlaid on the raw BOS image.

5.3 Acoustic Phased Array

A phased array of microphones was deployed to capture source distributions for the noise of the nozzle systems. A slightly smaller version of the OptiNav™ (OptiNav, Inc.) Array48 phased array was deployed on the wedge wall adjacent to the NATR. Four wedges were removed from the wall and a frame was mounted to the plywood backing of the wall, level with the model. The mounting bracket allowed horizontal angle adjustment so the array could be aimed along the jet axis. The array itself sat roughly a 0.5 m behind the tips of nearby wedges. (Wedges are 0.7 m tall.) The wedges above the array shielded the far-field microphones from any reflection off the array and its mounting hardware. In its final position, the array was 2.34 m from the jet centerline. A photo of the installed phased array is given in Figure 22.

The phased array consists of 48 Earthworks™ (Earthworks, Inc.) electret microphones arranged in a series of five log-spirals and flush mounted to a 1 by 1 m aluminum plate. Although these microphones have a flat amplitude frequency response out to only 30 kHz, the phase response can provide reliable source location data out to 48 kHz. During this test, data were acquired at each operating condition (each combination of setpoint and nozzle configuration) by simultaneously sampling the output of the 48 microphones at 96 kHz for at least 45 s. A camera mounted behind a window located in the center of the array plate was used to take a photo of each nozzle configuration that was tested.

The phased array data were processed using Beamform Interactive software from OptiNav™. The data were processed using Beamform Interactive's "fsweep" (short for frequency sweep) option, which outputs a stack of images, with each image in the stack corresponding to a different frequency band. Each image shows a contour plot of the source location data superimposed on top of a photo of the corresponding hardware configuration. These images are known as beamform maps. The location of the contour peak in the beamform map corresponding to a given frequency band denotes the location of the loudest source occurring in that band. The data were processed using 1/12th octave bands centered from 500 Hz to 44.7 kHz, resulting in stacks containing 79 images. Although this software package provides the choice of a number of different processing methods, conventional, time-domain, delay-and-sum beamforming was used to process the data presented in this report. This method assumes that the noise originates from uncorrelated point sources.

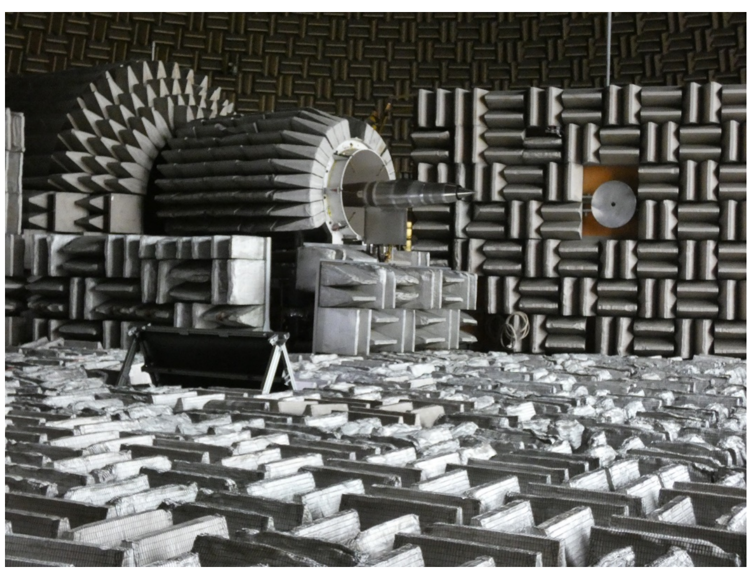

Figure 22.—Phased array embedded in wedge wall. Tilt mount attached with horizontal adjustment for aiming at axial target. Array is shielded from overhead microphones by overhanging wedges.

5.4 Installation Checks

The installations of the measurement systems were designed to put hard surfaces either in-plane with the far-field microphones, behind wedges from the microphones, or to be small enough to present negligible reflection. A CAD rendering of spatial locations of the instrumentation systems is shown in Figure 23. When the far-field microphone array, the phased array, and the BOS systems were all in place, an omnidirectional, spatially coherent speakerball was placed just downstream of the nozzle exit and its signature recorded at the far-field microphones with various elements of the BOS and phased array removed and in place. See Figure 24. The signals were analyzed both in spectral domain and by looking at the appropriate time delay in the autocorrelation given the expected reflection paths. Differences of less than 0.5 dB were found in all cases. Thus, it was established that the instrumentation produces less than 0.5 dB of error on the far-field measurements, a value within the expected uncertainty of the rig.

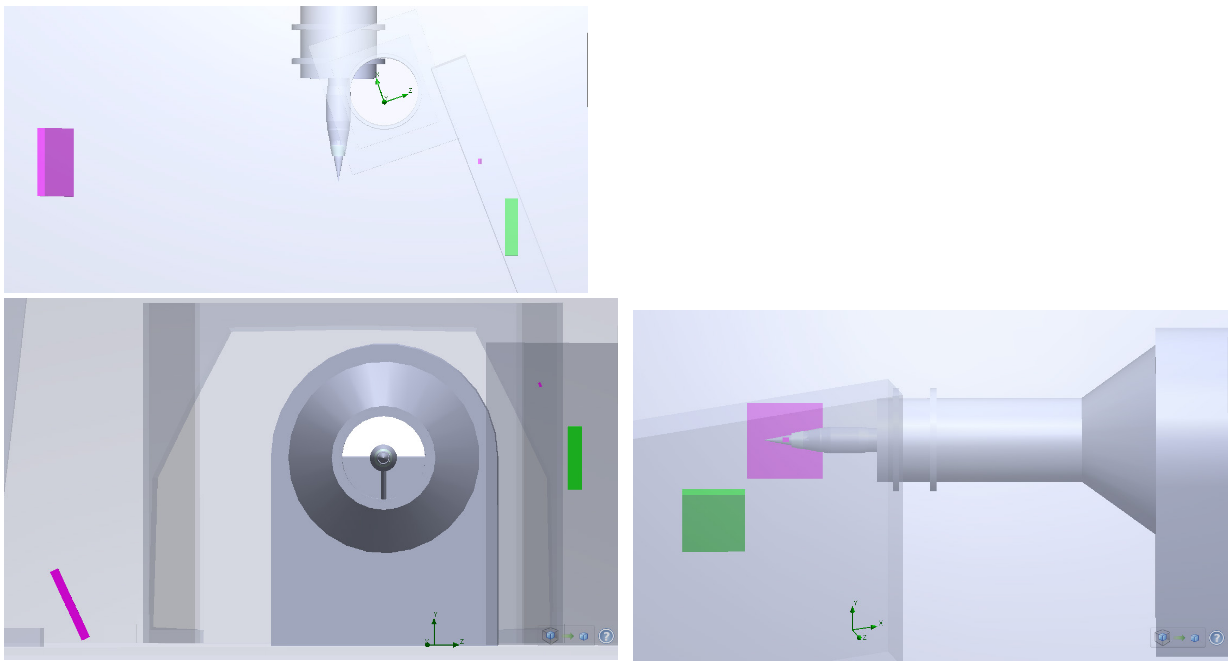

Figure 23.—Locations of phased array (green), and BOS background and camera (magenta) to minimize reflections from jet plume to overhead array. BOS camera and phased array located in wedge wall.

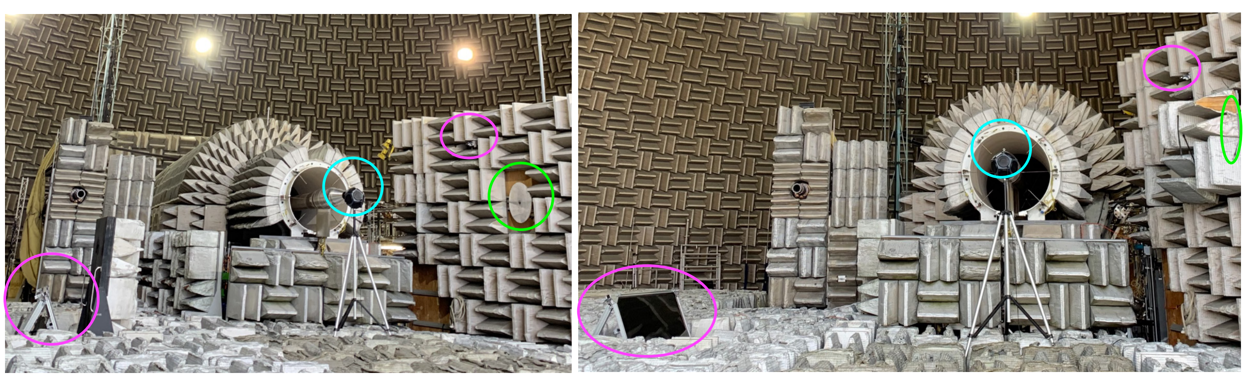

(a) (b)

Figure 24.—Diagnostic speakerball test to measure reflections from instrumentation. Speakerball circled in blue BOS camera and monitor circled in pink, phased array circled in green. In photo (a), BOS monitor is covered by a portable wedge wall while the phased array is uncovered. In (b), the BOS monitor is uncovered while the phased array is covered by wedges strapped in front of it.

6.0 Test Plan

Although there are 21 possible configurations from the interchangeable hardware parts, only 15 were planned to test and only 7 were actually tested during the abbreviated test. BOS and Array48 were used simultaneously with the far-field microphones. The tests were conducted over four days. During an 8-hr shift, it was possible to complete two configurations over the throttle line, and the order of model changes did not affect time for model change. Note that the unheated BBSN flow matrix (Table 5) was only run with configuration *122Am0pInt*.

7.0 Test Narrative

7.1 Facility Checkout

Although the first day of testing was scheduled for 18 March, facility preparation and model hardware delivery allowed installation to start 1 March. By 9 March all systems were essentially in place. Run days were to be from 8:00 to 14:00.

The first two days of facility availability (9-10 March) were used to confirm that the BOS and phased array hardware did not impact the far-field microphone measurements. This was done in two ways. First, an omnidirectional (spatially coherent) speakerball was put just downstream of the nozzle and far-field microphone signals were acquired with the BOS and phased array equipment exposed and with them covered by wedges. Autocorrelations of the microphone signals were inspected and compared. The expected signal in the autocorrelation at the delay time computed by the reflected paths was not found. In fact, the autocorrelations with and without the potential reflecting surfaces covered were indistinguishable. This indicates that the reflected energy is at least 10 dB below the directly transmitted energy.

The second way the facility setup was evaluated was simply by demonstrating that the jet rig was reproducing established acoustic signals for a reference jet flow. For this, the *122Am0pInt* nozzle was run with both streams matched at an unheated Ma = 0.9 (Tanna setpoint 7) condition. Far-field results of the 6in-diameter simple round jet were compared with scaled data from the 2in-diameter SMC000 nozzle acquired on the Small Hot Jet Acoustic Rig (SHJAR) as documented in Reference 7. The resulting spectra at 90° and 150°, scaled to the 6 in.-diameter are shown in Figure 25. The datasets agree within ±0.5 dB up until 10 kHz. As one of the concerns would be whether the wake of the internal splitter might be making noise, both the axisymmetric splitter *m0* and the *m5* lobed mixer were tested, each having a different wake. The results are identical, removing this potential noise source as a cause for any discrepancy between the NATR and SHJAR datasets. The cause of the difference above 10 kHz is not known at this time but is thought to be related to internal boundary layer differences or other Reynolds number dependencies.

Having determined that the rig was performing to specifications and that the BOS and phased array equipment were not influencing the far-field acoustic data, data acquisition for the test matrix was commenced on 11 March.

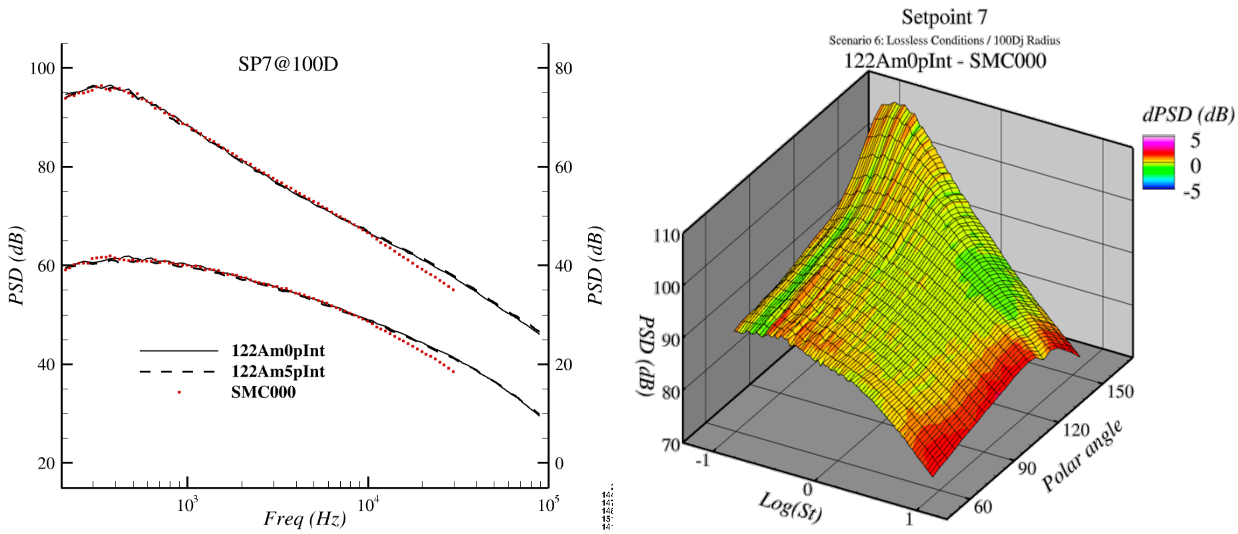

Figure 25.—Far-field acoustic PSD of simple round jet at unheated *Ma* = 0.9, lossless and scaled to r/D = 100. Data from internal plug Plug20 configurations compared with rescaled data from SHJAR SMC000 nozzle.

7.2 11 March 2020

Configuration: *122Am0pInt*. After a static background reading was acquired, the unheated matrix (Table 5) was acquired. This included Tanna setpoints 3, 5, and 7 along with the supersonic points to observe onset of broadband shock noise (BBSN). Central air services was alerted to provide 150 psi for the NATR, and after background readings were taken at *Mf* = 0.2 and 0.3 the engine matrix (Table 3) was acquired. It was a solid first test day with no issues being found; testing ran from 09:45 to 12:48.

7.3 12 March 2020

Configuration: *122DLm0p2068*. Testing started at 09:00 with a static background and one unheated setpoint (SP7). Background readings at *Mfj* = 0.2 and 0.3 were acquired, followed by the engine matrix. This finished at 11:15, and rather than acquire the BBSN matrix the model was changed. One clear observation: the nozzle was howling.

Configuration: *122DLm5p2069*. Testing continued after a change in mixer and plug, which took roughly 2 hr from shutdown to on-point. An unheated SP7 point was acquired, but the DataMAX was not armed and this was not caught until the model burner was lit—there is no acoustic data for SP7 on this configuration. The engine matrix was acquired in roughly an hour, finishing at 14:32.

7.4 13 March 2020

Configuration: *122DLm5p2079*. Overnight examination of data showed that uncovered screw holes on the plug were likely causing a whistle (not the nozzle howl seen in 122DLm0p2068). Starting today the screw holes were covered using nichrome patches tack-welded to the plug. The whistle, which was most evident in the SP7 data, was found to be gone. Testing started at 09:00 with a static background and one unheated setpoint (SP7). Background readings at *Mfj* = 0.2 and 0.3 were acquired, followed by the engine matrix. This finished at 10:40.

Configuration: *122DLm5p2068*. After a change in plug, testing resumed at 11:45. The unheated SP7 point was acquired (note that it is not completely unheated as the residual heat of the rig made the TTR = 1.09, not 1.0!). The engine matrix was acquired, finishing at 12:49.

7.5 17 March 2020

Configuration: *122Am5pInt*. On what proved to be the last run day before COVID19 shut down the test, testing started at 09:00 with a static background and one unheated setpoint (SP7). Background readings at *Mfj* = 0.2 and 0.3 were acquired, followed by the engine matrix. This finished at 11:15.

Configuration: *122DSm5p2069*. After the duct length was shortened, testing resumed at 12:45. The (almost) unheated SP7 point was acquired, but it appears that the acquisition was not completed before the rig flow settings were changed. Due to the urgency of completing the dataset before the center was shut for quarantine, the point was not retaken. The engine matrix was acquired, finishing at 14:00.

The test was working very efficiently when it was shut down by the quarantine of the Center. All instrumentation systems appeared to be working well, and the BOS data was processed and delivered by 16:00 of the last test day.

8.0 Results

Data analysis is ongoing at the time of this report, but some highlights of the data are given in this section.

8.1 BOS Data on Shocks

The Real-Time-BOS system enabled real time display of the density gradients (shocks) in the flow during the operation of the test hardware. BOS image data were also streamed to disk during the testing for post processing using higher fidelity data reduction techniques. Nominally, 200 BOS images were acquired at each set point in the test matrix. The image data were post-processed using the LaVision™ DaVis Least Squares Matching (LSM) based data reduction software. The BOS image data were first corrected for any physical shift between the reference images acquired before the tests began and the images acquired during rig operation. The BOS image data were then processed using DaVis' LSM processing using 15x15 pixel subregions size over a 7x7 pixel grid. The nominal scale factor for the BOS system was 0.3 mm/pixel. A mask is used in the BOS data processing in order to limit the region of the acquired images that actually contain flow information. The mask is typically drawn around the reference image. However, the BOS images acquired during the operation of the rig depict the thermal growth of the model from the reference image condition. At times there is a blank region around the edge of the model and the processed data field, which is due to the growth of the model beyond the mask region defined using the reference image. Use of the "hot" model image reduces this blank region. The on-condition image data also show that the model sometimes "droops" compared to the reference image location.

Ensemble averages of the individually processed density gradient maps were computed, yielding the derivatives of density in both the x-, y-coordinate directions. The processed BOS results represent the measured shifts in pixel units in the background optical pattern caused by optical refraction through density gradients in the flow. These measured shifts qualitatively represent the strong density gradients along the integrated path of the BOS system, and illustrate the location of shocks in the flow. There are two data files in each processed BOS directory (Appendix C) where the "Avg Vx" and "Avg Vy" variables correspond to the average density gradient values in pixel units along the x and y-direction, respectively. The file directory names reflect the processing steps applied to the data by the DaVis software. Results presented here are given as the average shift in the axial coordinate, comparable to a vertical (normal to the jet axis) knife edge in conventional Schlieren visualization.

BOS results are shown in Figure 26 for an internal nozzle (*122Am0pInt*) for the unheated flow matrix (Table 5). Note that flow is from right to left. The multiple flows presented in this figure show the onset of shocks in the simple plume and are comparable to those found in published historical datasets. The dataset at Mid < 1.01, with no shocks, gives the background 'noise' level of the method. The image at Mid = 1.01 picks up the very slight shocks present within the first diameter of the jet plume.

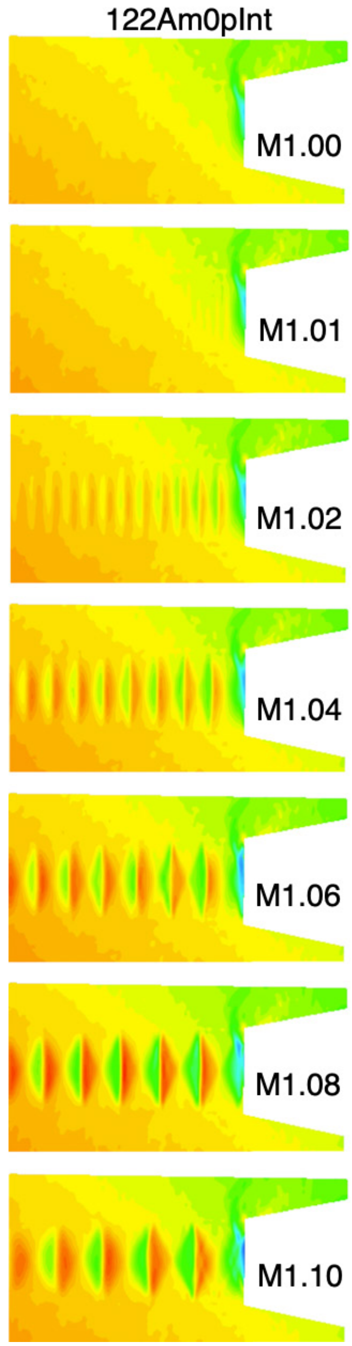

Figure 26.—BOS 'shocks' (axial shift in background pattern, dI/dx) for unheated BBSN sweep (single-stream matrix). *122Am0pInt*. Flow from right to left.

When the BOS instrumentation is applied to the internal plug nozzle with axisymmetric splitter *m0* running the engine matrix (Figure 27), the unmixed internal shear layer is easily visualized. Shocks form at setpoint 1203 (NPR = 2.0) and are stronger in the core stream. However, as the pressure ratio is increased the shocks can be seen in both streams, at the same spacing, with a small defect at the shear layer. When the same nozzle has a lobed mixer (*m5*) there are some axial streaks from imperfectly mixed thermal gradients, but the shocks are much more uniform across the jet. The shocks seem softer in the core than the unmixed case. The blue/red blotches at the nozzle exit in two of the plots of Figure 27 are instrumentation artifacts.

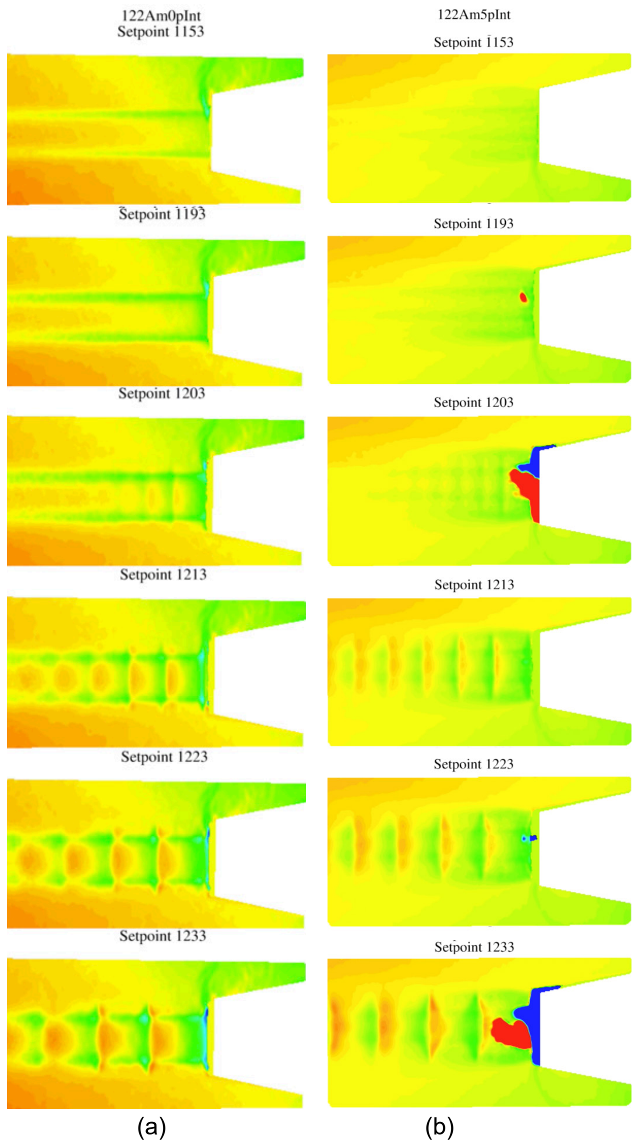

Figure 27.—BOS 'shocks' (dI/dx) over engine matrix for (a) *122Am0pInt*, (b) *122Am5pInt*.

One of the main reasons BOS was deployed in this test was to measure the shocks on the external plug. These shocks form at what should be subcritical nozzle pressure ratios because of the curvature of the flow over the crown of the plug. As shown in Figure 28, there are axial density gradients detected just downstream of the annulus opening of *122DLm5p2068* even at setpoint 1153. Here, the nozzle pressure ratio is 1.5 and gas Mach number is 0.79! This single gradient grows in strength through setpoint 1193, after which it is joined by further shocks as the pressure ratio increases until it has a full string of shocks extending well past the *p2068* plug by setpoint 1233.

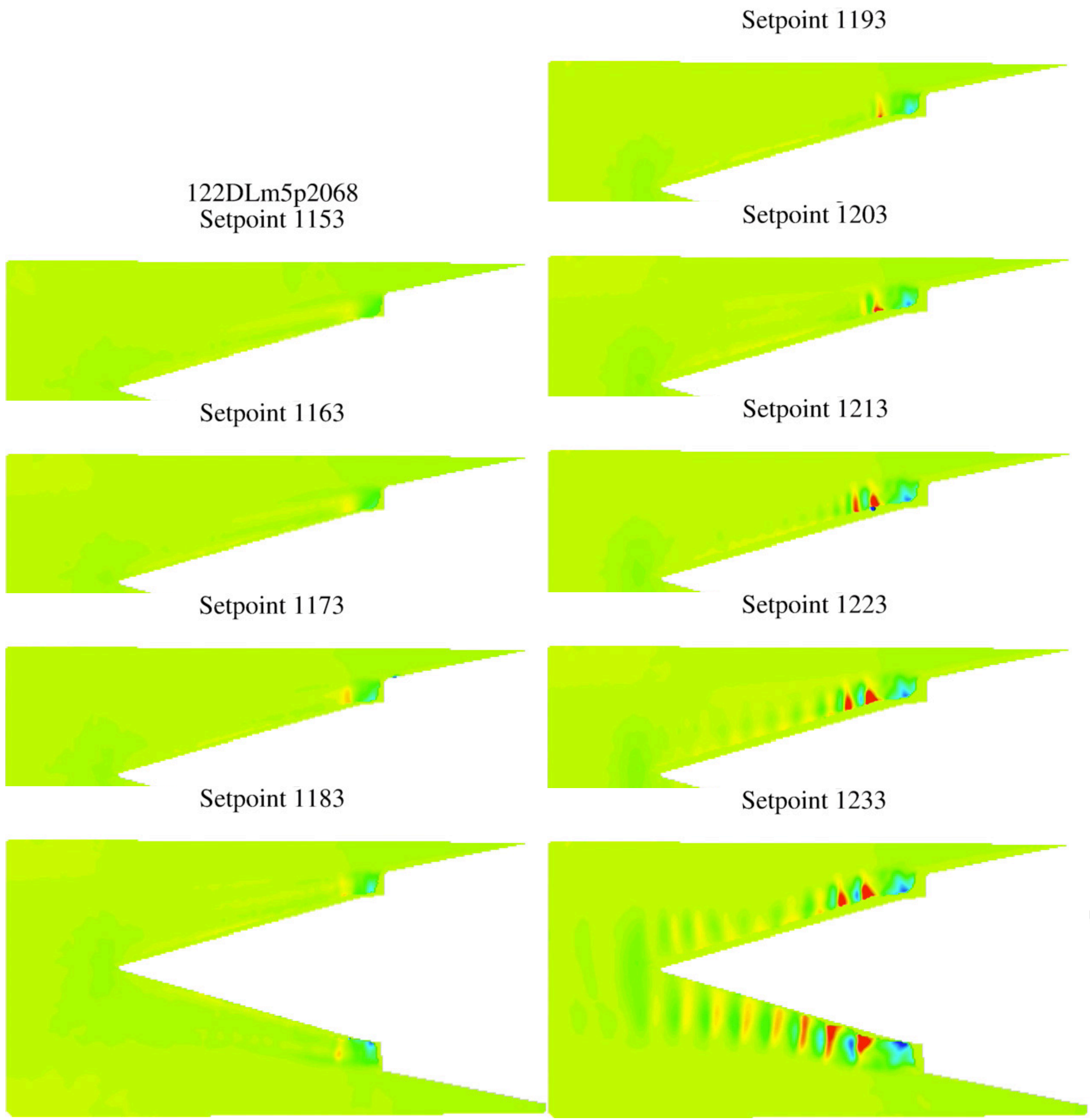

Figure 28.—BOS ‘shocks’ (dI/dx) for engine matrix on nozzle *122DLm5p2068*.

Part of the test design was to vary plug parameters, such as curvature smoothness (*p2068* vs. *p2069*) and plug length (*p2069* vs. *p2079*), in an effort to determine what noise was related to the shocks. Figure 29 compares the shock fields measured by BOS for these different plugs (and no plug) at setpoint 7. At this condition the two streams are matched both in pressure and temperature, making the plug geometry (not the mixer) the only difference. Inspection of the figure shows that the differences in the shock fields are very small. Features that are not the same on both sides are suspect, and there was a small asymmetry due to sagging of the plug. From the BOS figures, it does appear that *p2068* has one larger shock cell while *p2069* and *p2079* have two smaller ones. Reminder: Plug *p2068* had an abrupt change in curvature from the constant radius crown to a straight cone, whereas *p2069* and *p2079* had a gradual change in curvature. The results are not as dramatic as expected from CFD where the *p2069* and *p2079* designs had a much weaker shock than *p2068*. Also, the shocks appear stronger on *p2069* than *p2068*, opposite of what was predicted by CFD and counter to the changes noted in the far-field sound.

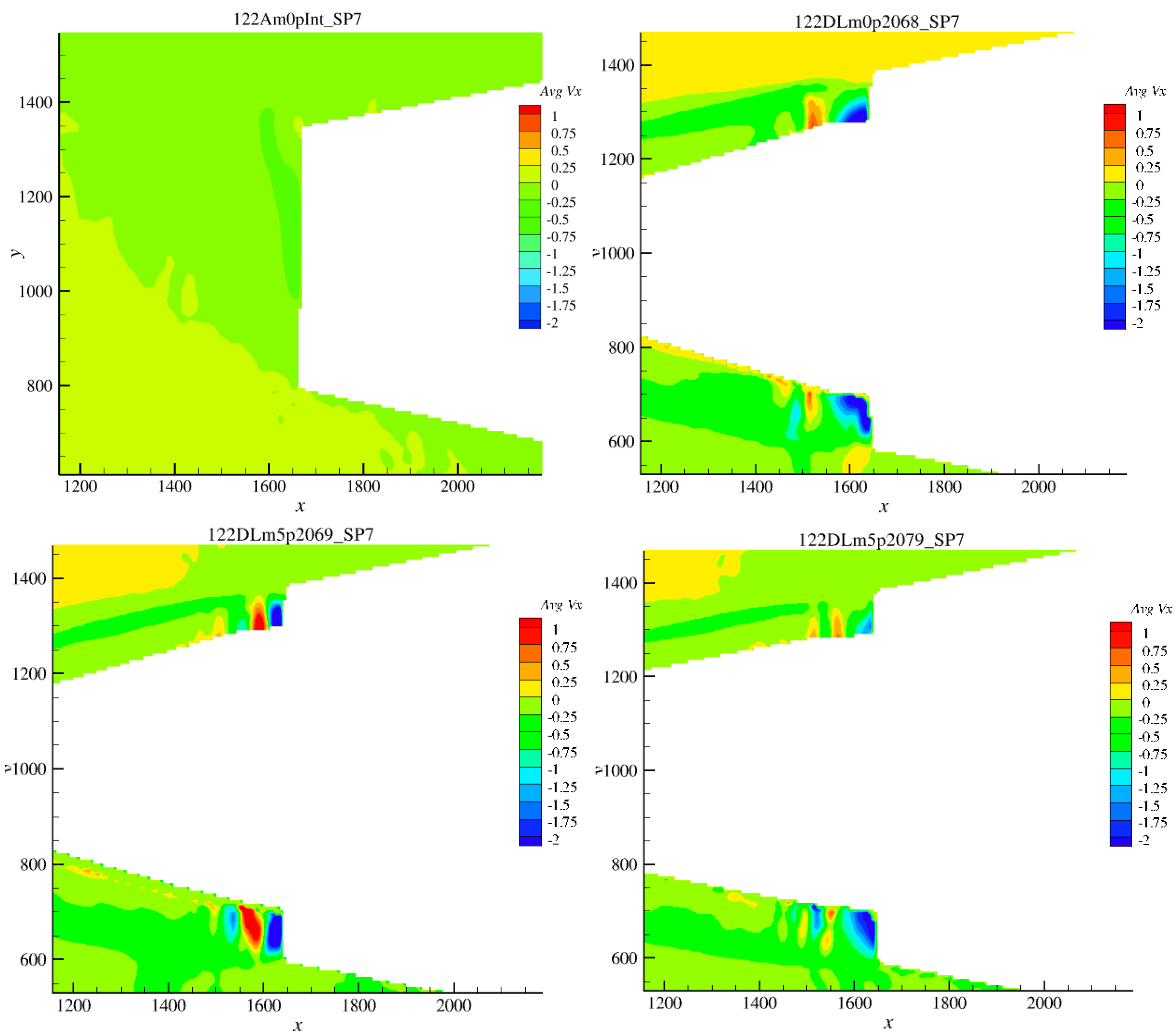

Figure 29.—BOS shocks in unheated, *Ma* = 0.9 (SP7) on flows from internal plug nozzle and external plug nozzles with different plugs.

8.2 Phased Array Measurements of Acoustic Source Distributions

When processed, phased array results are a three-dimensional map of source strength in two physical dimensions and frequency. They are best analyzed by comparing results of different configurations or flow conditions side-by-side, one frequency at a time. And because the source maps typically only have an dynamic range of 10 dB down from their peak values, the peak value printed in the upper corner of the maps must be considered when making the visual comparisons. In the figures to follow, the source maps are accompanied by line plots showing the power spectral density versus frequency of a central microphone in the array and showing the axial location relative to the nozzle of the highest peak in the source distribution as a function of frequency. The frequency scale is logarithmic in both plots. In both line plots, the frequency of the accompanying source map is denoted by a red asterisk. When a series of source maps are shown for different frequencies, the line plots are all the same but with the red asterisk moving to show the frequency of each source map.

Figure 31 shows a comparison of source maps for internal and external plug nozzles, both run with unheated, matched streams at *Ma* = 0.9 (setpoint 7). In the figure, only 6 frequencies are shown (each covers a 1/12-octave band), but in the processed data there are maps for 82 1/12-octave frequency bands from 500 Hz to 53 kHz. The most obvious difference was between 4 and 8 kHz. In the internal plug nozzle, the source continuously shrank in size and moved toward the nozzle exit as the frequency was increased. In the external plug nozzle, the source bifurcated around 4 kHz into two sources, one roughly at the end of the potential core and one on the plug. These two regions traded energy as frequency is increased until by 8 kHz the downstream source was 10 dB below the upstream source. This behavior has been noted in other recent tests of external plug nozzles (Ref. 8), but this is the first time that the phenomena has been documented in back-to-back comparisons with an internal plug nozzle, removing the possibility that the phased array setup was to blame.

Source maps in Figure 30 were acquired with the axisymmetric internal mixer *m0* in the internal and external plug configurations. As the flow conditions were matched in both streams, it would seem that the type of internal mixer should not matter. However, the presence of the lobed mixer may have left residual cross-stream velocity gradients (axial vortices) even as the two streams had the same total conditions and hence no internal shear from mismatched stream conditions. Figure 31 therefore compares the same two nozzles but with the *m5* internal mixer. Comparisons of Figure 30(a) and Figure 31(a) confirm that the internal mixer had no impact on the measured source maps for the nozzle with internal plug. However, for the external plug nozzle there was a difference around 4 kHz even though the flow should have been identical and the far-field spectra were essentially the same (at frequency St = 2 in Figure 37). This observation is made easier by direct comparison of the source maps of *122DLm0p2068* and *122DLm5p2068*, given in Figure 32, a direct comparison of Figure 30(b) and Figure 31(b).

Returning to the comparison of internal versus external plug configurations, only now at an engine flow condition with unmixed flows, Figure 33 compares the source distributions of *122Am0pInt* and *122DLm0p2069* at setpoint 1203. At this supercritical flow condition (NPR = 2.0) the internal plug nozzle showed evidence of broadband shock noise (BBSN) as the peak source location shifted up and down stream with increasing frequency. This has been observed in single-stream shocked jets (Ref. 9). The external plug configuration, however, did not have these nonmonotonic shifts in source location with frequency. The *122DLm0p2069* configuration did have a strong resonance producing a peak in noise at roughly 1.2 kHz, but at this low frequency the phased array did not see a significant change in location—it was too poorly resolved by the array.

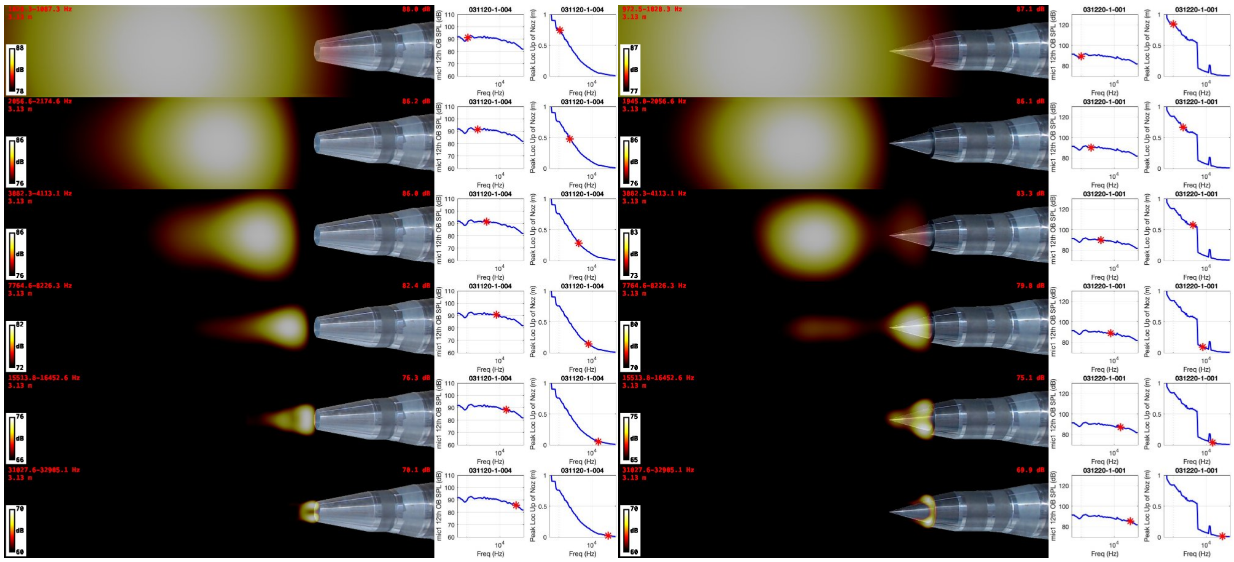

Figure 30.—Acoustic source distributions as measured by phased array. Setpoint 7 flow from (a) *122Am0pInt*, (b) *122DLm0p2068*, at frequencies (from top) 1, 2, 4, 8, 16, and 32 kHz.

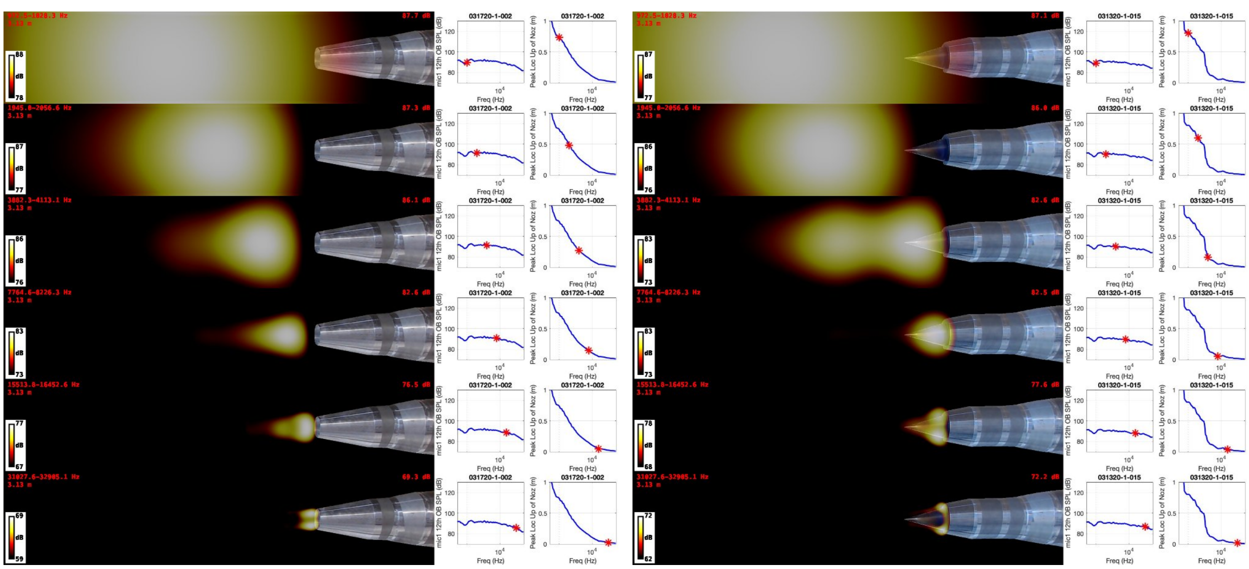

(a) (b)

Figure 31.—Acoustic source distributions as measured by phased array. Setpoint 7 flow from (a) *122Am5pInt*, (b) *122DLm5p2068*, at frequencies (from top) 1, 2, 4, 8, 16, and 32 kHz.

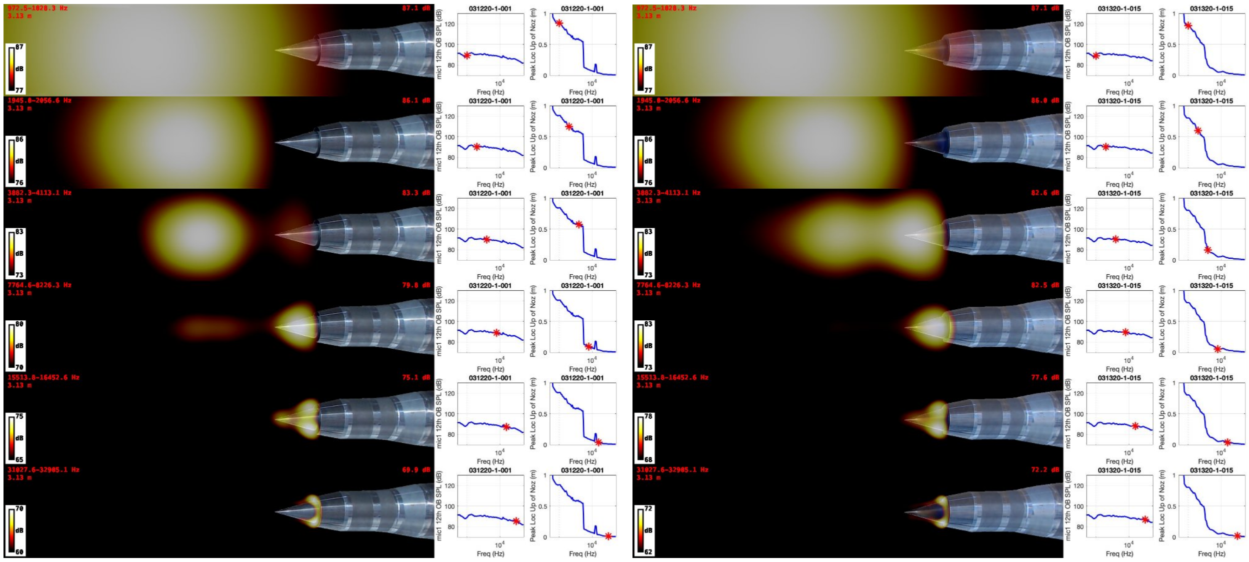

(a) (b)

Figure 32.—Acoustic source distributions as measured by phased array. Setpoint 7 flow from (a) *122DLm0p2069*, (b) *122DLm5p2068*, at frequencies (from top) 1, 2, 4, 8, 16, and 32 kHz.

When a lobed mixer was used on the same two nozzles shown in Figure 33, it made surprisingly little difference to the source distribution of the external plug nozzle, but it did make a significant difference to that of the internal plug nozzle, as shown in Figure 34. The nonmonotonic shift of the peak noise location up and down stream observed with the *122Am0pInt* nozzle associated with the broadband shock noise is replaced by a conventional behavior of simple jet mixing in the *122Am5pint* configuration. This, in spite of the presence of shocks being clear in BOS schlieren of both configurations shown in Figure 27. This comparison is made easier by putting the datasets side by side, as in Figure 35. Two possible explanations present themselves. First, judging from the BOS data, the *m0* had an energetic inner shear layer interacting with the plume shocks, while the inner shear layer of the *m5* mixer had largely dissipated, possibly leaving the BBSN source much weaker. Second, the peak values of the *122Am0pInt* and *122Am5pInt* maps differ significantly. The *122Am5pInt* peak values in the high frequency bands where the BBSN would be evident are 5 to 9 dB higher than those of *122Am0pInt*, meaning there may have been BBSN sources in the *122Am5pInt* plume, but they were overshadowed by the higher mixing noise of this configuration.

Finally, three different external plugs were tested and their source distributions at 20 kHz at the takeoff condition of setpoint 1203 are directly compared in Figure 36. The distributions at first seem very similar, but the peak amplitude difference in the plots for the two short plugs is significant. The *p2068* plug had a 4 dB higher amplitude and was more compact on the plug, roughly where the flow was predicted to separate. The *p2069* plug had a more diffuse source distribution over the entire plug. The long *p2079* plug had a distribution very similar to that of the *p2069* plug and was roughly 1 dB louder. The peak of the source distributions of both *p2069* and *p2079* plugs showed slightly nonmonotonic axial shift around 16 kHz, as observed in the line plots of peak location versus frequency in Figure 36.

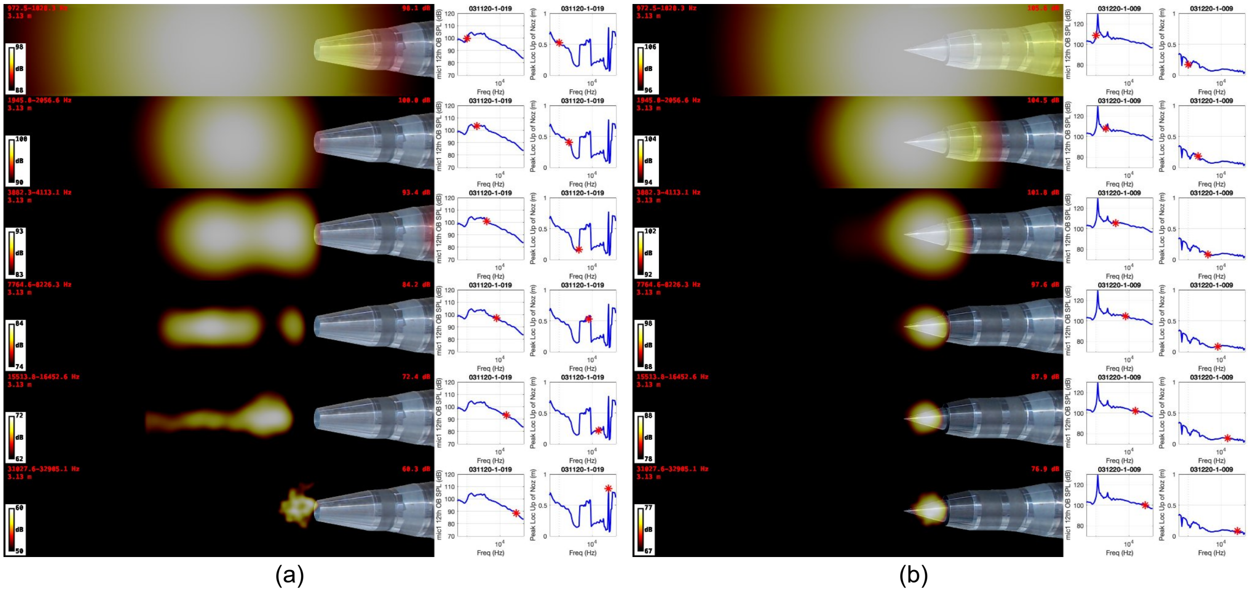

Figure 33.—Acoustic source distributions as measured by phased array. Setpoint 1203 flow from (a) *122Am0pInt*, (b) *122DLm0p2069*, at frequencies (from top) 1, 2, 4, 8, 16, and 32 kHz.

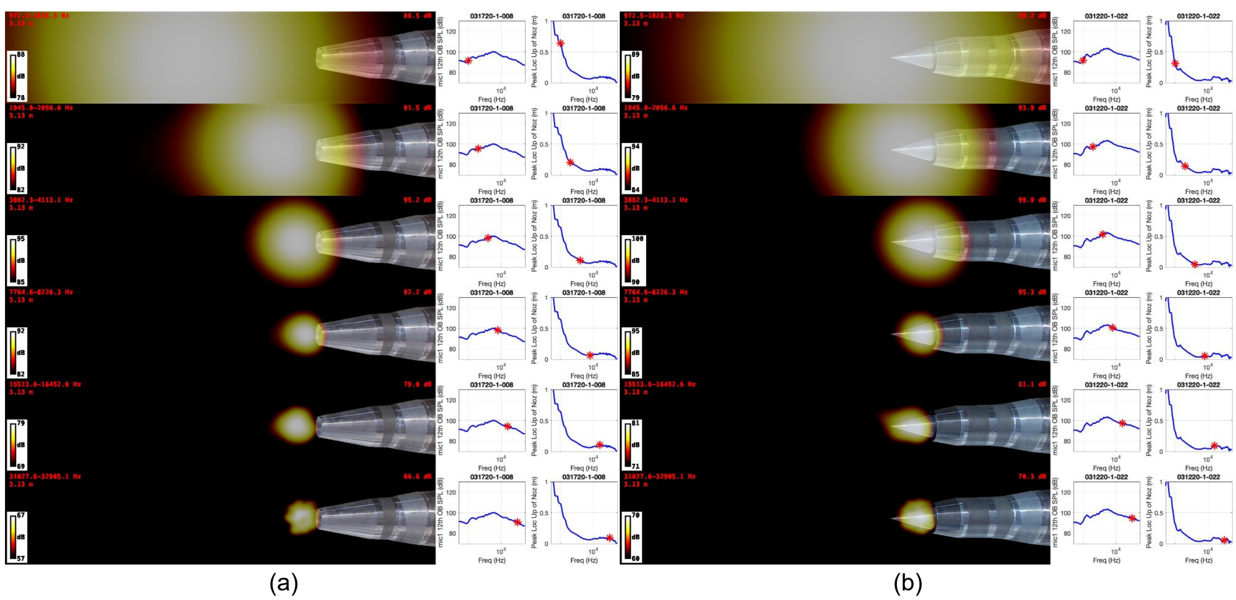

Figure 34.—Acoustic source distributions as measured by phased array. Setpoint 1203 flow from (a) *122Am5pInt*, (b) *122DLm5p2069*, at frequencies (from top) 1, 2, 4, 8, 16, 32 kHz.

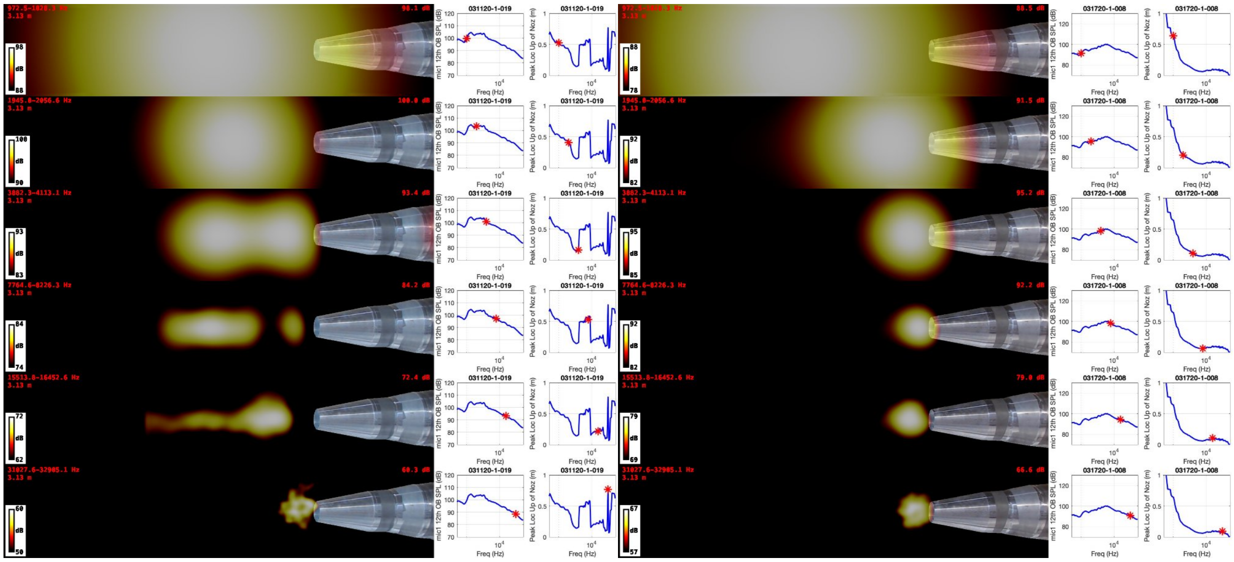

Figure 35.—Acoustic source distributions as measured by phased array. Setpoint 1203 flow from (a) *122Am0pInt*, (b) *122Am5pInt*, at frequencies (from top) 1, 2, 4, 8, 16, and 32 kHz.

(a)
(b)
(c)

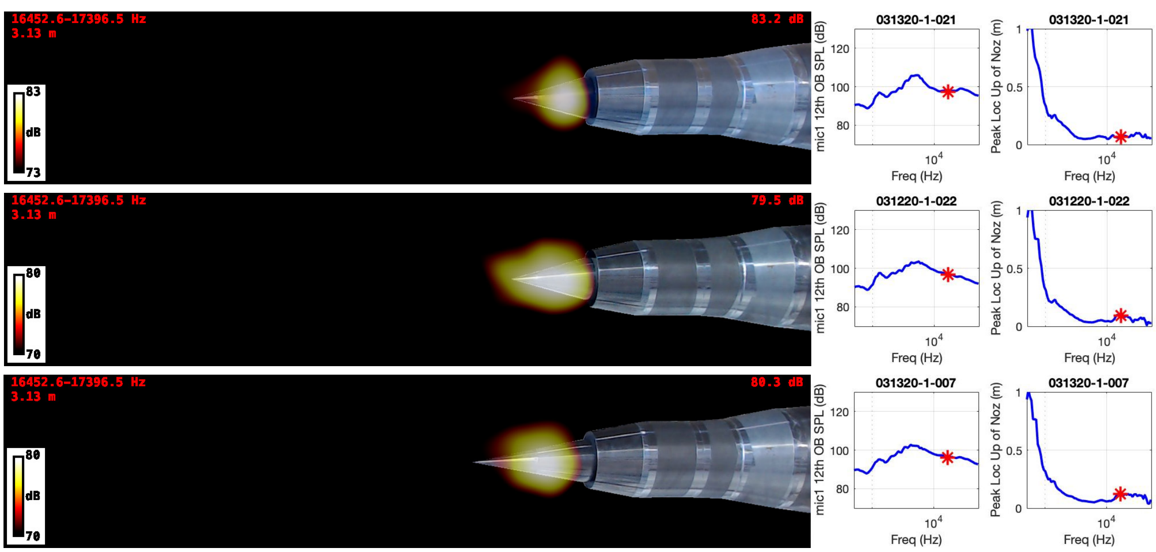

Figure 36.—Acoustic source distributions as measured by phased array. Setpoint 1203 flow from configurations with different plugs: (a) *122DLm5p2068*, (b) *122DLm5p2069*, (c) *122DLm5p2079* at 20 kHz.

8.3 Far-Field Acoustics

Far-field acoustic results have been processed to 1-ft lossless, source-centric conditions, accounting for shear layer refraction using the *djshear5.2* DADS routine. Far-field spectral directivity data, in model-scale, 1-ft, lossless scenario, are given in digital form in Appendix B.

8.3.1 Effect of plug shape (unheated, *Ma* = 0.9 flow)

One big question to be answered was whether external plugs with a fully mixed flow had a different noise than a nozzle with internal plug. Figure 37 documents that the presence of an external plug does not make a significant difference in the noise of an unheated, single-stream jet until the plug length is very long. Even then, the impact is only ~1.5 dB.

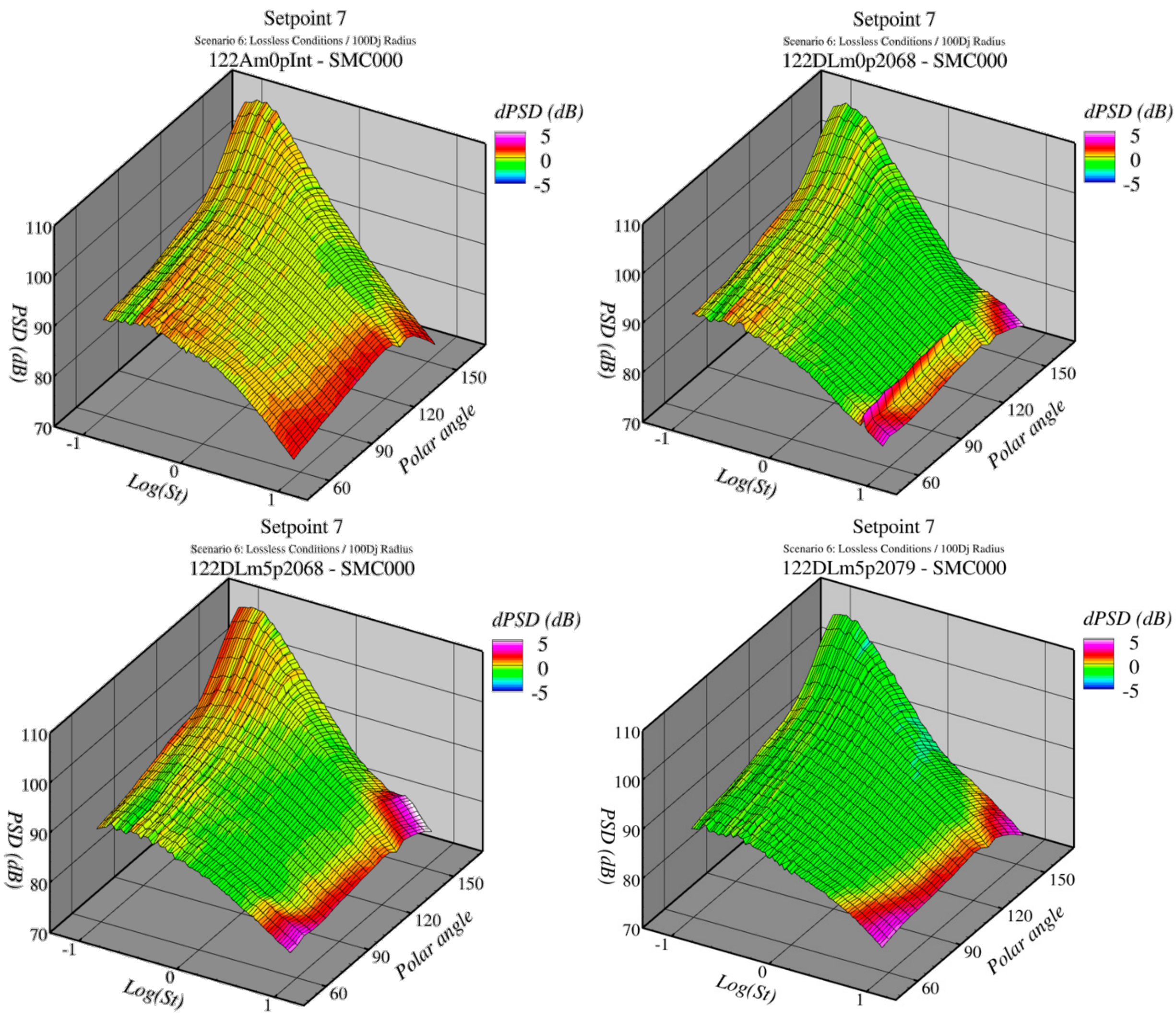

Figure 37.—Far-field (r/D = 100), lossless PSD as function of Strouhal number for four of the nozzles tested. Shape is PSD, color is delta-PSD from SMC000 nozzle data demonstrating rig independence and small variations caused by plug.

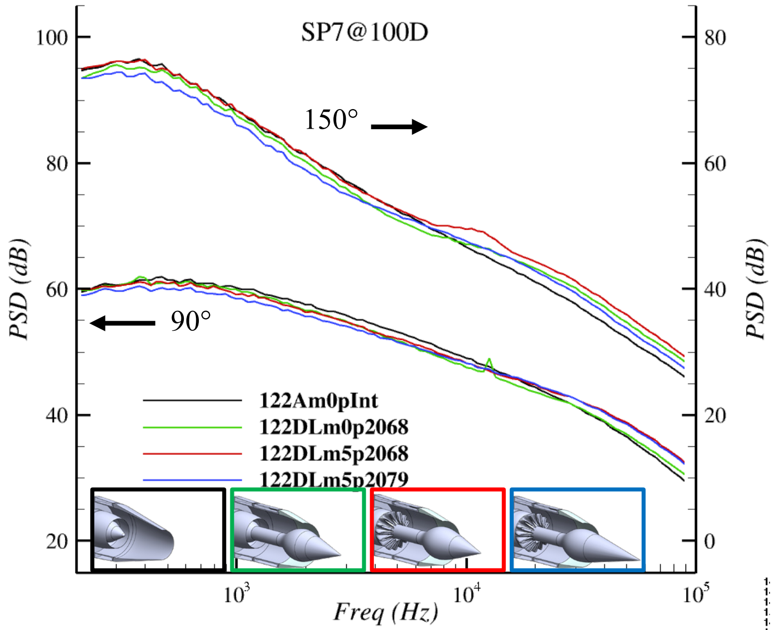

Figure 38.—Far-field PSD, scaled to r/D = 100 (lossless), for internal and external plug nozzles at unheated, *Ma* = 0.9 (SP7) flow condition. Spectra given at 90° and 150° polar angles.

In each plot in Figure 37 is given the spectral directivity of the jet noise of one of the Plug20 nozzles at setpoint 7 (unheated, *Ma* = 0.9), normalized to Strouhal scaling in frequency. The color contours depict the difference between the noise of the Plug20 nozzle and the SMC000 nozzle, a simple 2 in. diameter conic nozzle tested on SHJAR (Ref. 7). The two cases had a 3x scale factor difference, and a substantial difference in rig description. However, for the axisymmetric *122Am0pInt* nozzle the difference was less than ±0.5 dB over most of the frequency, polar angle domain. Frequencies above St = 10 were different, being a bit higher for the Plug20 nozzles. This is believed to be a Reynolds number effect, and is more clearly quantified in Figure 25. Over the range where the two rigs agreed for the internal plug nozzle, the external plug nozzles differed from the internal plug nozzle by as much as 1.5 dB quieter in the case of the long plug. Except for the long plug nozzle, the external plug nozzles matched the internal plug nozzle nearly to within experimental uncertainty. Detailed comparisons can be seen at 90° and 150° in Figure 38. The high frequency differences at the 150° angle are significant; the small tone observed in the *122DLm0p2068* spectrum at 90° is the whistle produced by the uncovered screw head on the plug, discussed in the test narrative above.

8.3.2 Onset of conventional broadband shock (BBSN)

Given that the subcritical shock on the external plug is suspected of being part of a noise mechanism, it is good to start with a review of BBSN as it is conventionally understood in nozzles without external plugs. It is also worthwhile to document that the internal plug nozzle obeyed the conventionally observed behavior. From this it can be seen (in the discussion below) that the spectral humps associated with the external plug nozzles with internal mixers differs from conventional BBSN.

Figure 39 presents far-field acoustic spectral directivities of the *122Am0pInt* nozzle with matched, unheated, streams. This resulted in a uniform unheated flow at the exit, and it is not surprising that as the nozzle pressure ratio was increased past critical $M = 1$ there was an onset of BBSN. In the figure, the BBSN is accentuated by coloring the contour maps with the difference between the measured sound and a simple model of the mixing noise. The latter is simply modeled by taking the sound of the $M = 1.00$ jet and increasing its amplitude by 80*$\log_{10}(M)$ to represent the mixing noise component of the higher *M* jets. Over this small range of *M*, the M^8 scaling is roughly held over all polar angles, making this a useful model for visualizing the added noise of the BBSN component by removing the mixing noise component. The line plot in the figure allows precise comparisons of the different *M* for a 60° observer where the BBSN is most dominant over the mixing noise component. In the figure, the spectra have monotonic roll-off until *M* = 1.02 (NPR = 1.938). At this flow condition there is a very slight hump at 6 kHz. At successively higher *M* the hump appears at lower frequencies: 4.7, 3.5, and 3.2 kHz. Again, this is in keeping with conventional understanding of BBSN where the frequency is inversely proportional to the shock spacing.

It is also worth noting that the shock patterns measured by BOS associated with each of the jet flows given in Figure 39 are given in Figure 26.

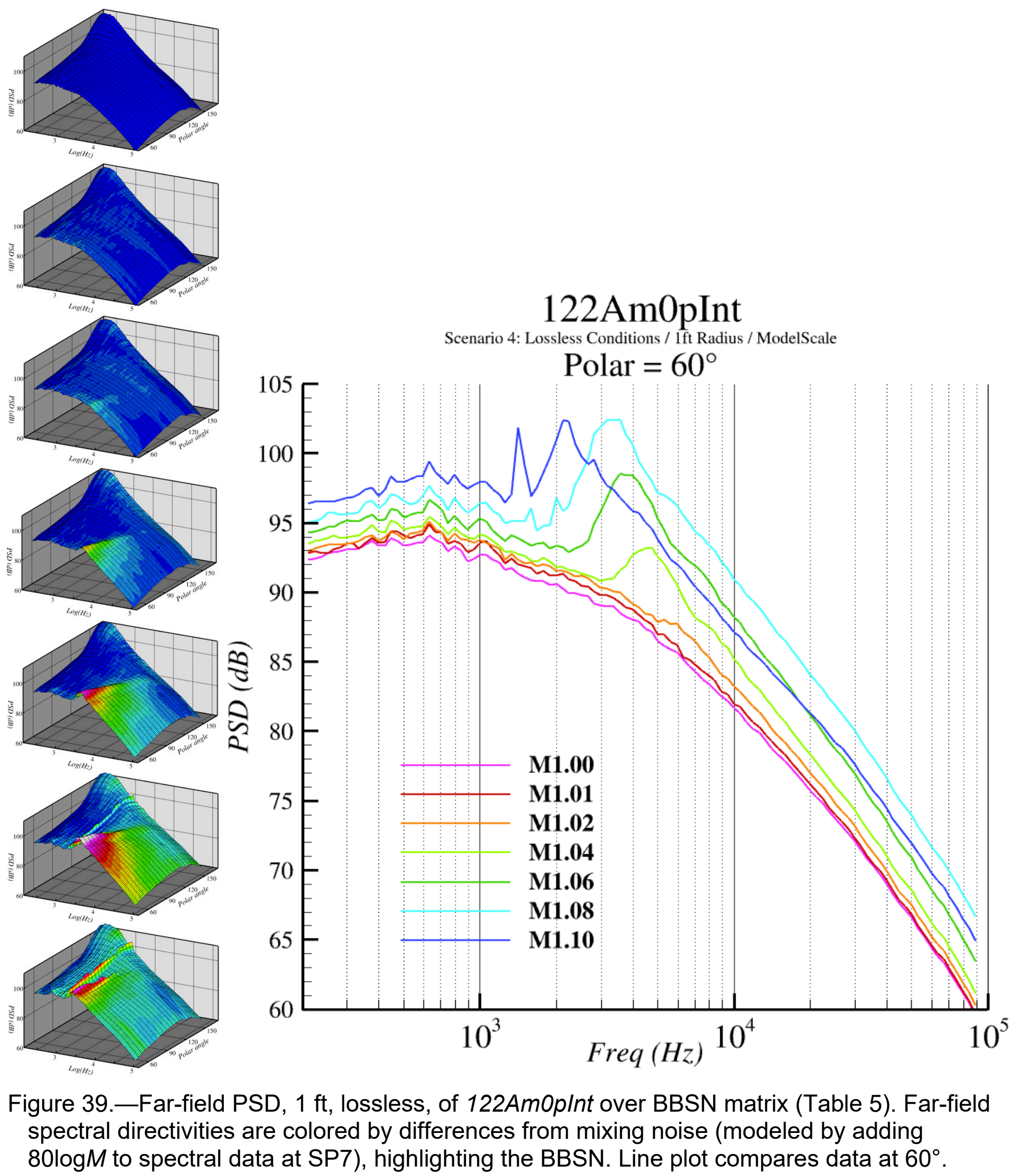

Figure 39.—Far-field PSD, 1 ft, lossless, of *122Am0pInt* over BBSN matrix (Table 5). Far-field spectral directivities are colored by differences from mixing noise (modeled by adding 80log*M* to spectral data at SP7), highlighting the BBSN. Line plot compares data at 60°. Corresponding BOS data are given in Figure 26.

8.3.3 Onset of BBSN in internally mixed nozzles

Once the core flow was heated, the shock pattern for the internal plug nozzle became more complicated, depending upon the internal mixer, as shown in Figure 27. The corresponding changes to the far-field acoustic spectra at 60° are shown in Figure 40. Polar angle 60° was chosen for the plot as this is where the BBSN is strongest relative to the mixing noise.

For the axisymmetric splitter (Figure 40(a)), the spectra at frequencies above the peak in mixing noise had a near-linear decay with frequency for subcritical pressures ratios (SP1153-1183). There was a hint of a hump at 3 kHz at SP1193 and 1203, but the hump became very significant at the highest three flow conditions. Note how the peak frequency of these last three humps shifted significantly with NPR, consistent with conventional BBSN; the humps at the transitional setpoints 1193 and 1203 did not. Conventional BBSN would have had humps at much high frequency than those observed at these two transitional setpoints. Therefore, it seems these humps were probably not related to the BBSN mechanism observed at the highest setpoints.

When a lobed mixer was present (Figure 40(b)), the spectra had a subtle hump or change in slope around 6 kHz for all the subcritical setpoints, which was present until setpoint 1203. The change between setpoints 1203 and 1213 was dramatic, with a spectral hump appearing at 3.2 kHz and shifting to lower frequencies with increasing pressure ratio. The behavior of these latter three points was the same as with the axisymmetric splitter and conventional BBSN. It is therefore surmised that the spectral features of the subcritical flows were not due to BBSN, but was instead related to the internal mixer.

When an external plug is present, it is more difficult to separate out the impact of the internal mixer from the shocks that appear on the plug, even in subcritical flow conditions. Figure 41 uses the same presentation format as Figure 40, only now for the configurations with external plug. As noted in the test narrative above, configuration *122DLm0p2068*, (Figure 41(a)) with the axisymmetric splitter, produced a flow with strong resonance. That this resonance is geometrically based is clear by the insensitivity of the

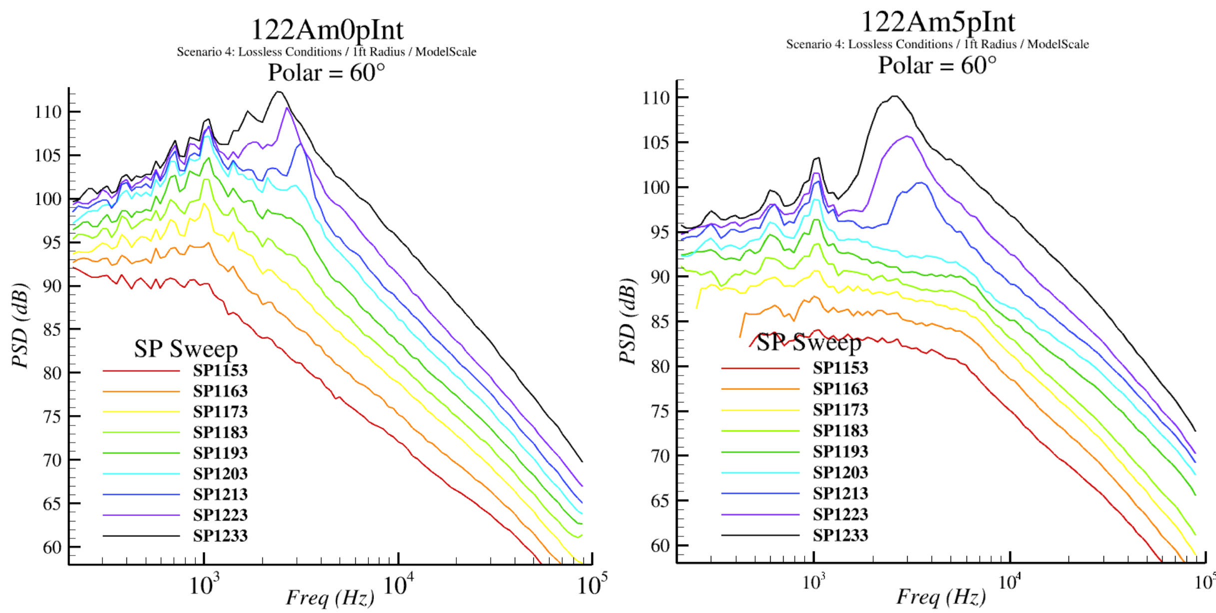

(a) (b)

Figure 40.—PSD at polar angle 60° over 1xxx matrix for (a) unmixed *122Am0* and (b) mixed *122Am5* nozzles. Polar angle 60° chosen to highlight onset of BBSN and its differences with the lobed mixer.

frequency to the flow condition. The spectra of the configurations with lobed mixers but different plugs are similar but have differences in the spectral hump in the 2 to 10 kHz range. The *p2068* plug produced a strong hump at all flow conditions than the other plugs, possibly associated with a difference in the curvature shocks over the plug. Differences between *p2069* and *p2079* plugs are more subtle at this polar angle, which may be attributed to the similarities in their profiles (Figure 12) near the shocks.

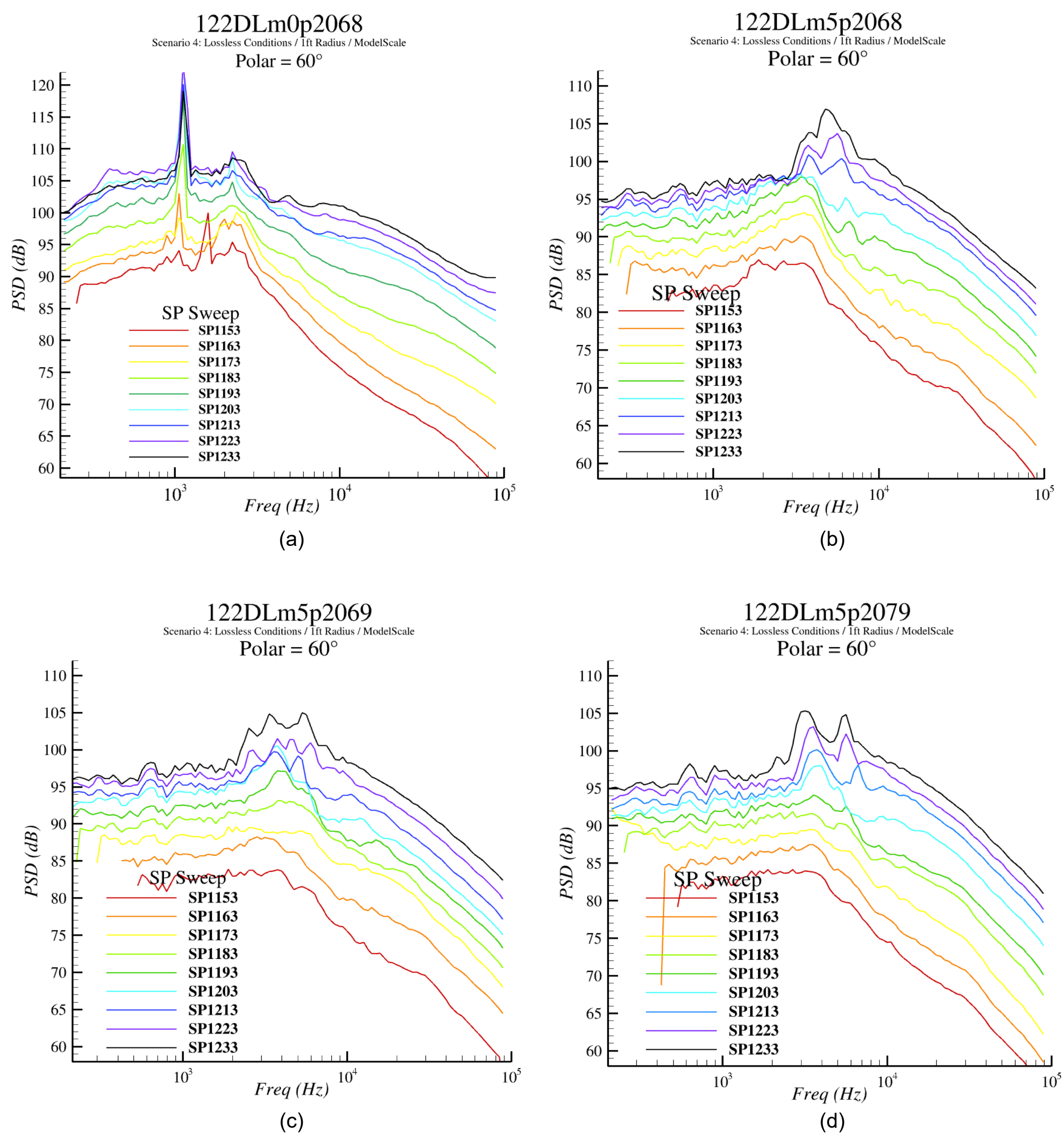

Figure 41.—PSD at polar angle 60° over 1xxx matrix for external plug nozzles: (a) unmixed *122DLm0p2068*, (b) mixed *122DLm5p2068*, (c) mixed *122DLm5p2069*, mixed *122DLm5p2079*. Polar angle 60° chosen to highlight onset of BBSN and its differences with the lobed mixer and plug design.

8.3.4 Differences in 'mixing noise' due to internal mixer, plug type

As it appears that BBSN is not a dominant noise source at setpoint 1203 (NPR = 2.0), and because this is a setpoint of interest to proposed commercial supersonic aircraft, a more detailed study will be made of the nozzles at this setpoint.

Direct comparisons of spectral directivity for the nozzles test is given in the next few figures. Figure 42 gives direct comparison of the spectral directivity of the internal plug nozzle with splitter versus lobed mixer, and external plug nozzle with splitter versus lobed mixer. Note that the external plug nozzle with splitter produced very large tones at a fixed frequency. These tones were very sharp in frequency, leading to the diagnosis of a resonance condition, possibly between the axisymmetric splitter and the nozzle lip. There was no resonance in this nozzle when the streams were matched (Figure 37), reducing the possibility that the tone is related to upstream rig sources or to external flow separations on the plug. This was the only configuration in this test that developed such a resonance. Feedback from the axisymmetric shear layer of the splitter impacting the nozzle lip is proposed as the mechanism, given that the tone was independent of flow condition (Figure 41(a)). When the lobed mixer was tested, the lack of azimuthal coherence of the shear layer at the nozzle exit (among other factors) probably precluded the resonance condition.

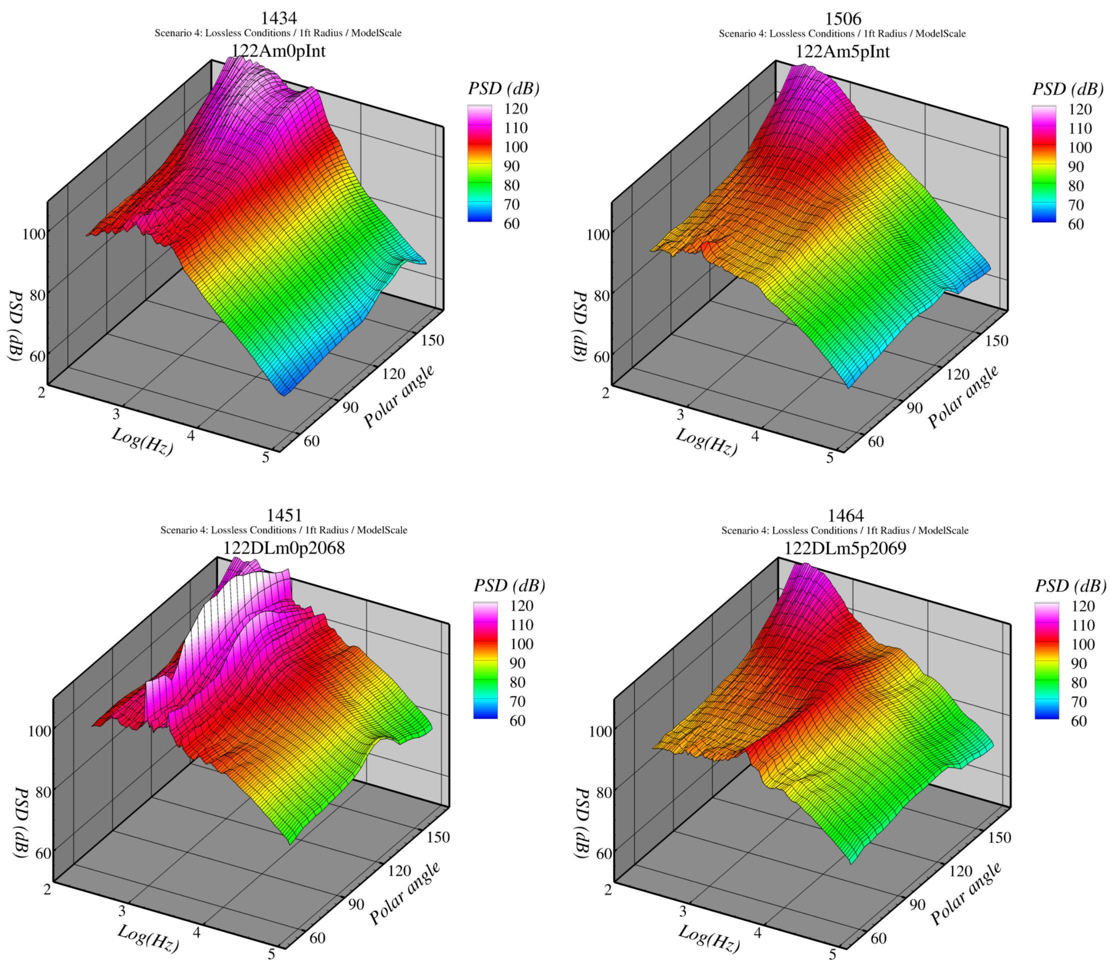

Figure 42.—Far-field PSD, 1 ft, lossless for key nozzle types: internal plug (top row), external plug (bottom row); axisymmetric splitter (left) and forced lobed mixer (right). Setpoint 1203.

A spectral hump was observed in the spectra of the internal plug nozzle flows, and this hump had different peak frequencies depending on the internal mixer. For the *m0* splitter, the spectral hump peaked at 3 kHz; for the lobed mixer it peaked at 6 kHz. For the splitter, the spectral hump amplitude increased with downstream angle; for the lobed mixer it reached its maximum in polar angle around 110°. There is further discussion of these observations below around Figure 46.

The comparison of mixers in the external plug nozzle was spoiled by the resonance in the splitter configuration, but comparison between the internal and external plug nozzles with lobed mixer is possible. The spectral hump in both cases had maximum amplitude roughly at polar angle 110° to 120°, and seemed to be in approximately the same frequency. Looking closer, *122Am5pInt* had a peak frequency of 5200 Hz; *122DLm5p2069* had a peak frequency of 4400 Hz. Whether this shift matched changes in turbulent lengthscales of the mixer shear layer as they accelerated out the nozzles has yet to be determined. In addition, the peak frequency of the hump generated by the external plug nozzle was not quite constant. More on this in the discussion around Figure 47.

8.3.5 Differences in far-field noise due to mixing duct length

One short duct configuration was tested: *122DSm5p2069*. Comparing the noise from this configuration with that of *122DLm5p2069* isolates the effect of mixing length between mixer and nozzle lips. Figure 43 makes this comparison for the spectral directivities of the two configurations. The most striking difference is the shift in the frequency of the spectral hump that dominates the high frequency sound of both configurations. The peak frequency at polar angle 110° is 4400 Hz for the long duct and 9500 Hz for the short duct. For reference, the distance between mixer and nozzle lips was 13.98 and 4.08 in. for the two configurations (Figure 14). Other observations are that all high frequencies above the spectral hump are elevated in the short duct configuration, and the dominant jet peak noise is slightly reduced.

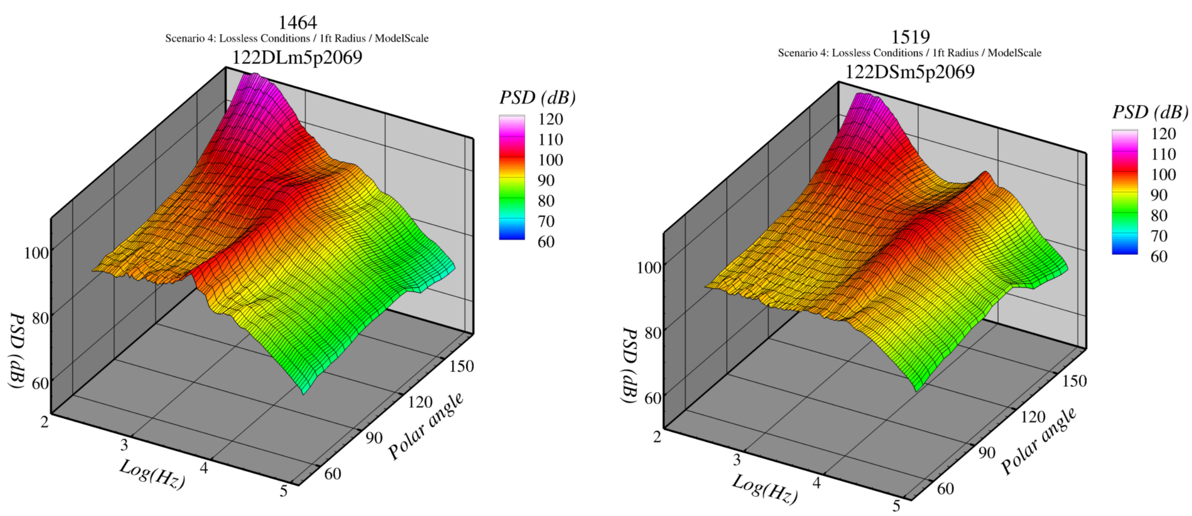

Figure 43.—Far-field PSD, 1 ft, lossless for external plug nozzles with long and short mixing ducts. Setpoint 1203.

8.3.6 Differences in far-field noise due to plug design and length

In initial studies of the external plug nozzle, the presence of shocks and potential separations on the plug were flagged as potential noise sources that had not been examined before. Changes in plug shape and length were tested with plugs *p2068*, *p2069* (different shape), and *p2079* (different length). Figure 44 documents the change in spectral directivity due to shape and length. For more precise measurement of the differences caused by the plug configurations, the noise of the lobed mixer with plug *p2069* is taken as a baseline configuration and differences (in dB) with the other configurations are calculated and displayed by color on the carpet plots.

The difference between *p2068* and *p2069* (plug shaping) has the spectral humps relatively the same, but the humps on the *p2068* plug were louder by 2 to 3 dB. There is evidence of a slight shift in the frequency of the main hump at the lowest polar angles, and the frequencies above the hump were higher for *p2068*.

The differences between *p2069* and *p2079* (plug length) were small, ±1 dB. The longer plug was slightly quieter over most frequencies and angles, except for at high frequencies and low angles where it was higher.

8.3.7 Discussion of results

A few key observations were made in processing the data from the Plug20 test. While more analysis will be required to fully understand these observations, some discussion is included in this test report.

One objective of the test was to see how internal and external plugs differ with internal mixers. One significant difference was the presence of subcritical shocks in the flow of the external plug nozzles. In analogy with conventional BBSN, it was assumed that these shocks convert turbulent energy convecting in the shear layer into noise. One clear indicator of BBSN, as seen in Figure 45, was how the spectral hump shifted frequency with polar angle. This is due to the kinematics of shear layer disturbances convecting over a fixed set of evenly spaced shocks, producing an array of coherent sources to steer the directivity of different frequencies. But in the subcritical shock of the external plug there was only one (maybe two?) shock cells. Does this produce a similar BBSN? Under the assumption that it does share the same characteristics as conventional BBSN, we look at the directivity of the humps in the far-field spectra.

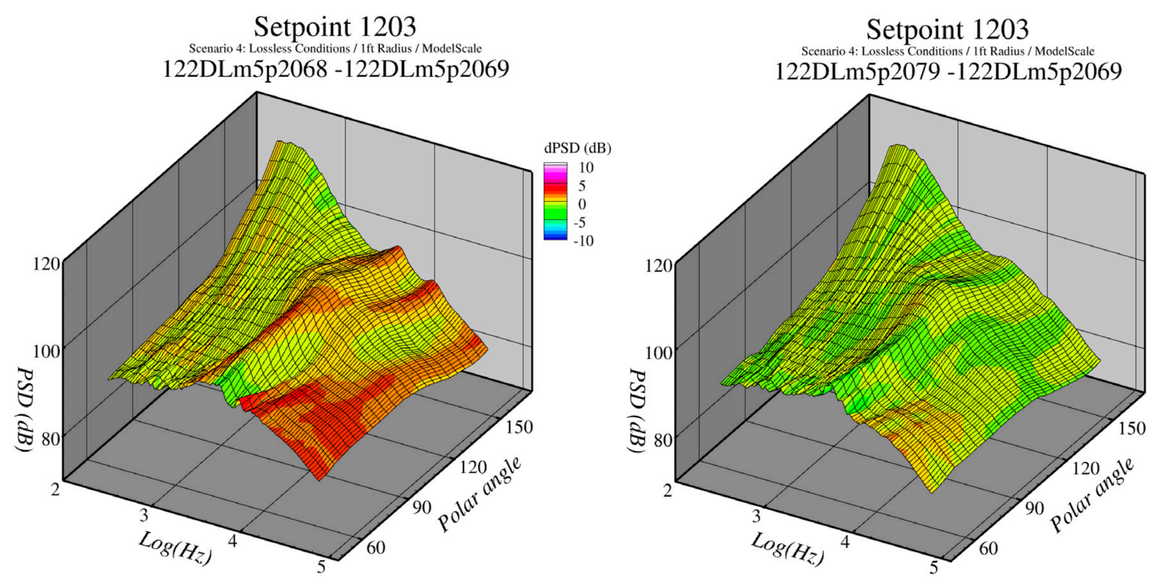

Figure 44.—Far-field PSD, 1 ft, lossless for external plug nozzles with different plugs. Setpoint 1203. Color indicates deviation, in dB, between plugs 2068-2069 (left), and plugs 2079-2069 (right).

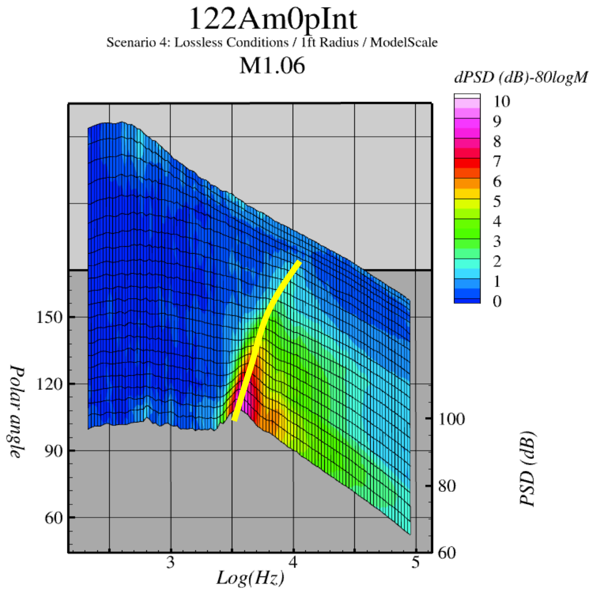

Figure 45.—Far-field PSD, 1 ft, lossless, of *122Am0pInt* at setpoint 405. Far-field spectral directivity is colored by difference from mixing noise (modeled by adding 80logM to data at SP7), thus highlighting the BBSN.

Start by noting that the external plug nozzles had the subcritical shock at setpoint 7 (Figure 29), and the far-field spectral directivity of the external plug nozzles was not louder, nor does it have a distinct hump, compared to the internal plug nozzle (Figure 37). This seems to indicate that the subcritical shock itself did not produce an additional noise source for the external plug nozzle, at least not when interacting with the nozzle shear layer.

Next, consider the humps that were observed in the case of unmixed flow, with and without the external plug, starting with the internal plug configuration.

At setpoint 1203, one setpoint before the onset of spectral humps identified as BBSN in the internal plug nozzle, there were spectral humps not associated with that of a fully mixed jet. With the internal plug, these humps had the same peak frequency over all polar angles (dashed lines in Figure 46). The change in peak frequency of the spectral hump in the internal plug data from a strong hump at 3 kHz in the case of the axisymmetric splitter *m0* to a subtle 5 kHz hump from the lobed mixer *m5* seems to implicate the splitter/mixer as the source of the hump in the internal plug nozzle cases. Also note that the spectral hump is maximum around polar angle 150° for the axisymmetric splitter *m0* and around polar angle 110° for the lobed mixer *m5*.

The resonance of the *122DLm0p2068* nozzle deprives us of having a direct mixer change for the external plug nozzle to isolate the influence of the mixer on the external plug nozzles. Only external plug configurations with a lobed mixer are available.

With the external plug and lobed mixer, the spectral hump did shift frequency with polar angle, much like the spectral humps produced by BBSN (Figure 47). This seems to indicate that the noise source is an array of broadband sources, like BBSN. However, the polar dependence of the humps was similar to that of the internal plug with lobed mixer, peaking around polar angle 120°. As a reminder, for conventional BBSN, the polar directivity is fairly uniform, typically being covered by the jet mixing noise as polar angle increases. The polar directivity of the hump in the noise of all nozzles with the lobed mixer tested here was rather sharp and was mirrored through the spectra at frequencies higher than the main spectral humps.

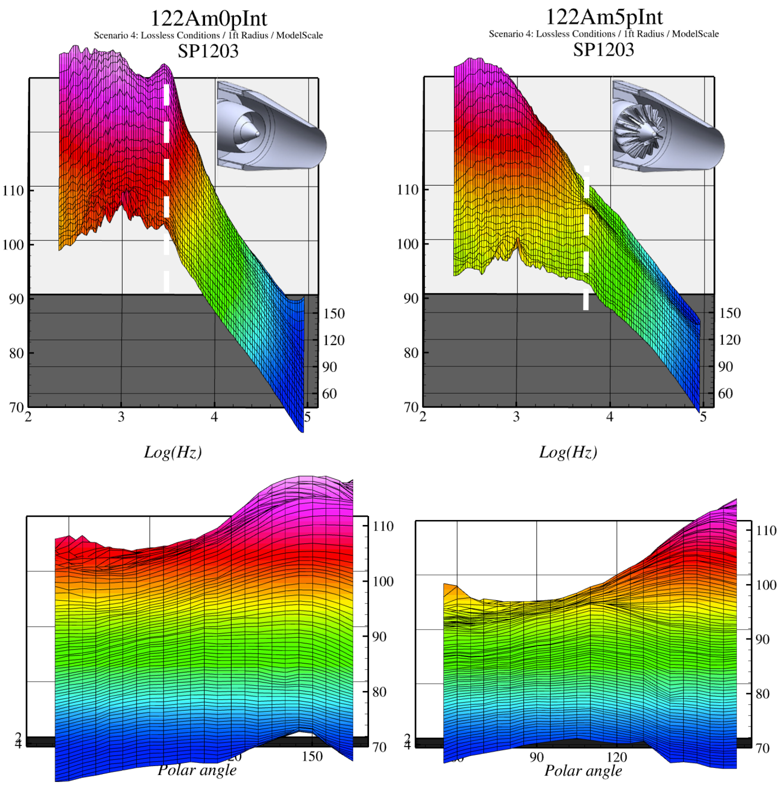

Figure 46.—Far-field PSD, 1 ft, lossless for internal plug nozzles with different mixers. Note that spectral ‘humps’ have same frequency over polar angle.

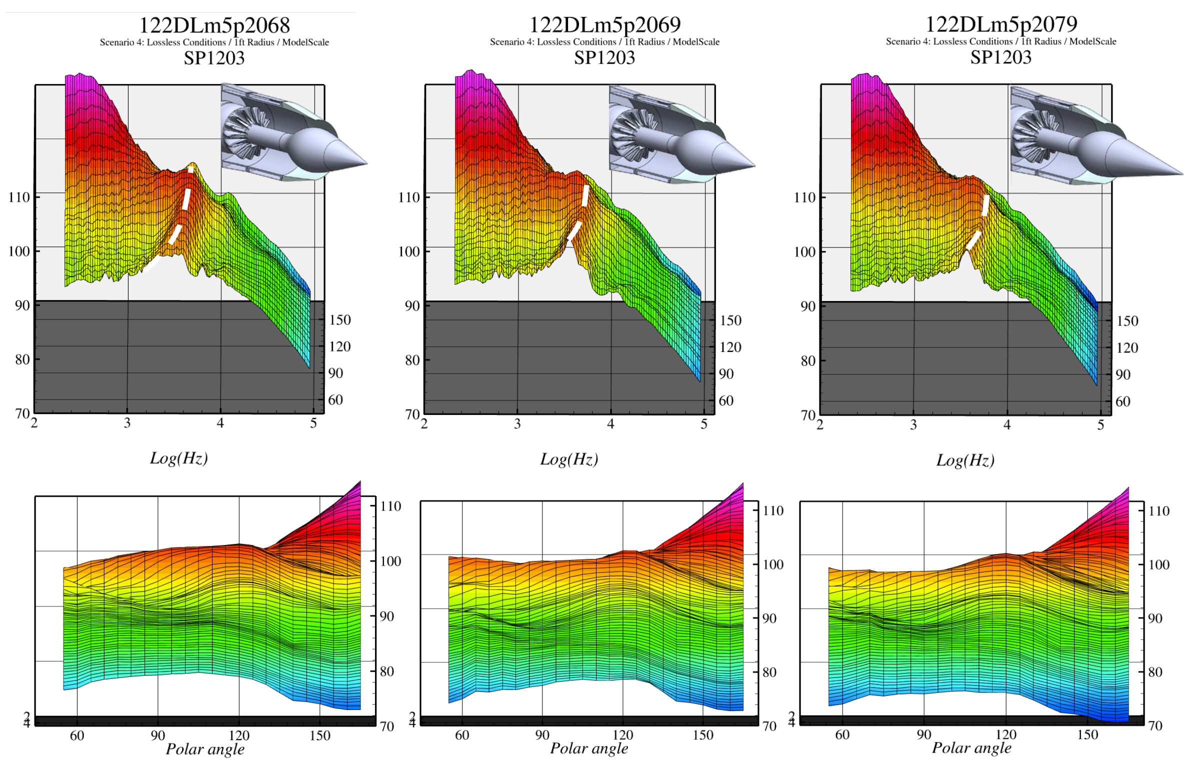

Figure 47.—Far-field PSD, 1 ft, lossless for external plug nozzles with different mixers. Note that some spectral ‘humps’ shift frequency over polar angle.

The conflicting characteristics of the spectral humps produced by the lobed mixers with external plug is possibly the most interesting observation from these tests. It seems to be associated with the turbulence produced by the internal mixer, but is the turbulent energy converted to acoustic energy by interaction with the nozzle lip, with the shocks of the plug, or something else?

8.3.8 Catalog of spectral directivities

Spectral directivities of all the configurations tests are presented in Figure 48 through Figure 54. In each figure, the upper left plot is setpoint 7 and subsequent plots (left-to-right) are setpoints 1153 to 1233. The data are PSD at 1 ft radius, lossless transformation including shear layer correction. The data for all these and more are included in digital format in Appendix B.

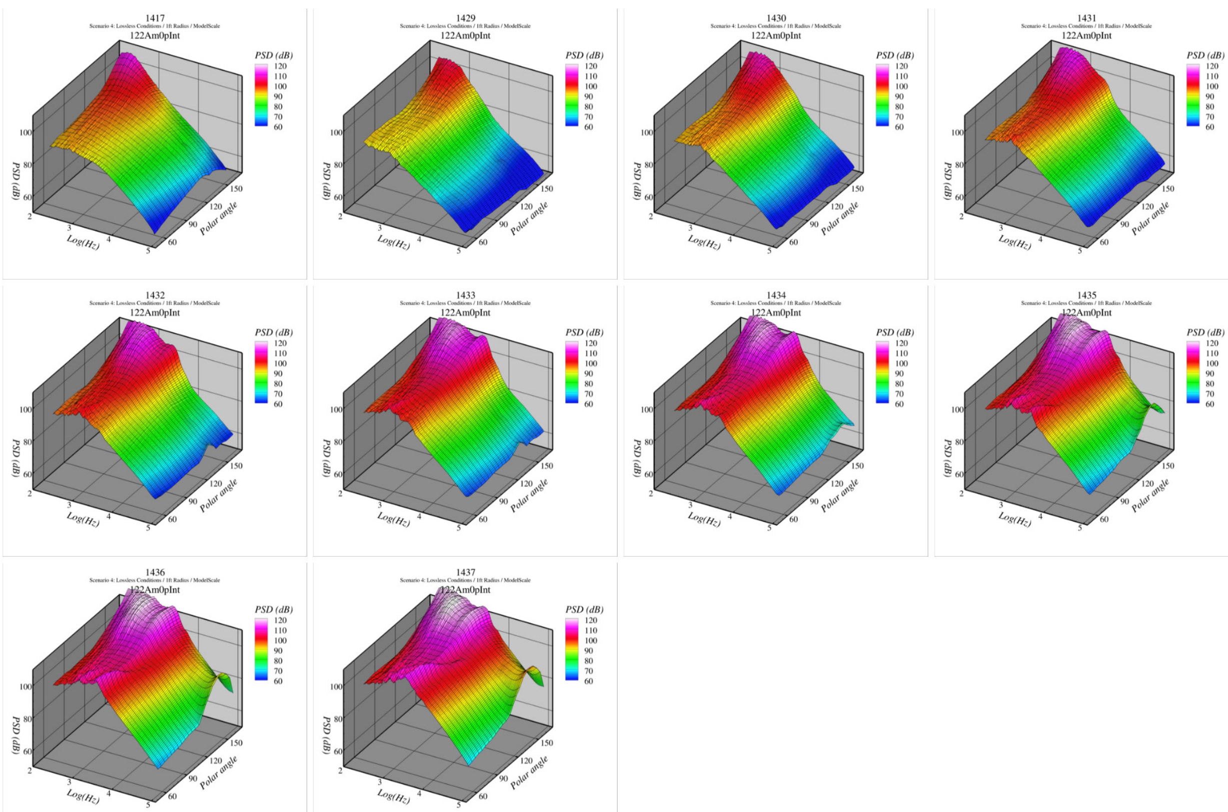

Figure 48.—Far-field PSD, 1 ft, lossless for *122Am0pInt*, SP7+ engine matrix.

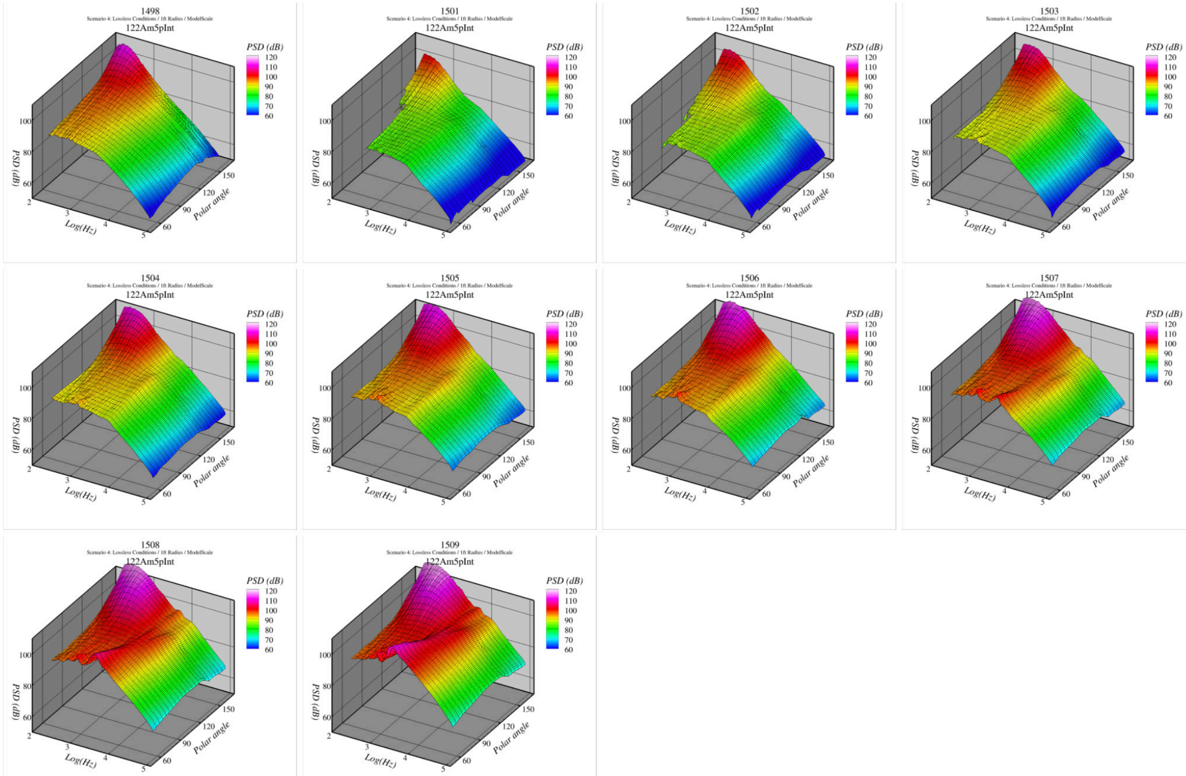

Figure 49.—Far-field PSD, 1 ft, lossless for *122Am5pInt*, SP7+ engine matrix.

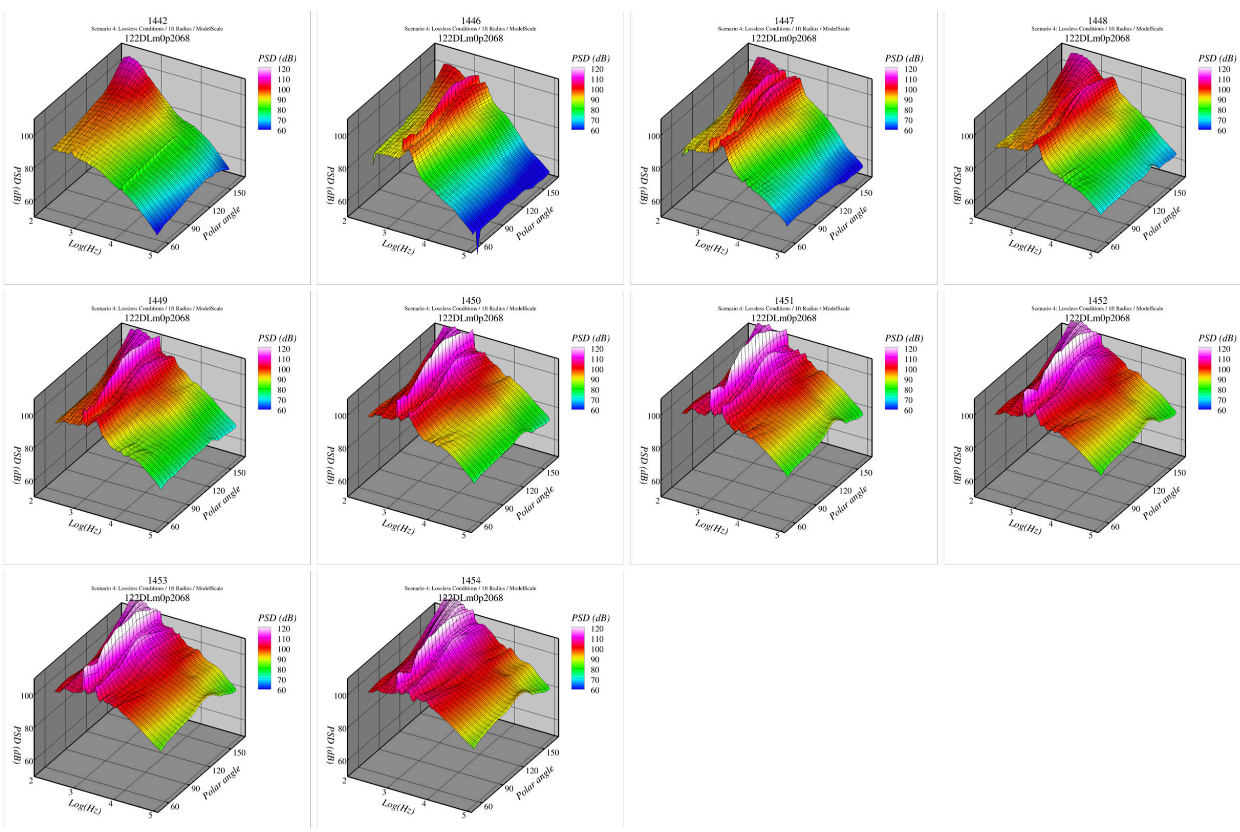

Figure 50.—Far-field PSD, 1 ft, lossless for *122DLm0p2068*, SP7+ engine matrix.

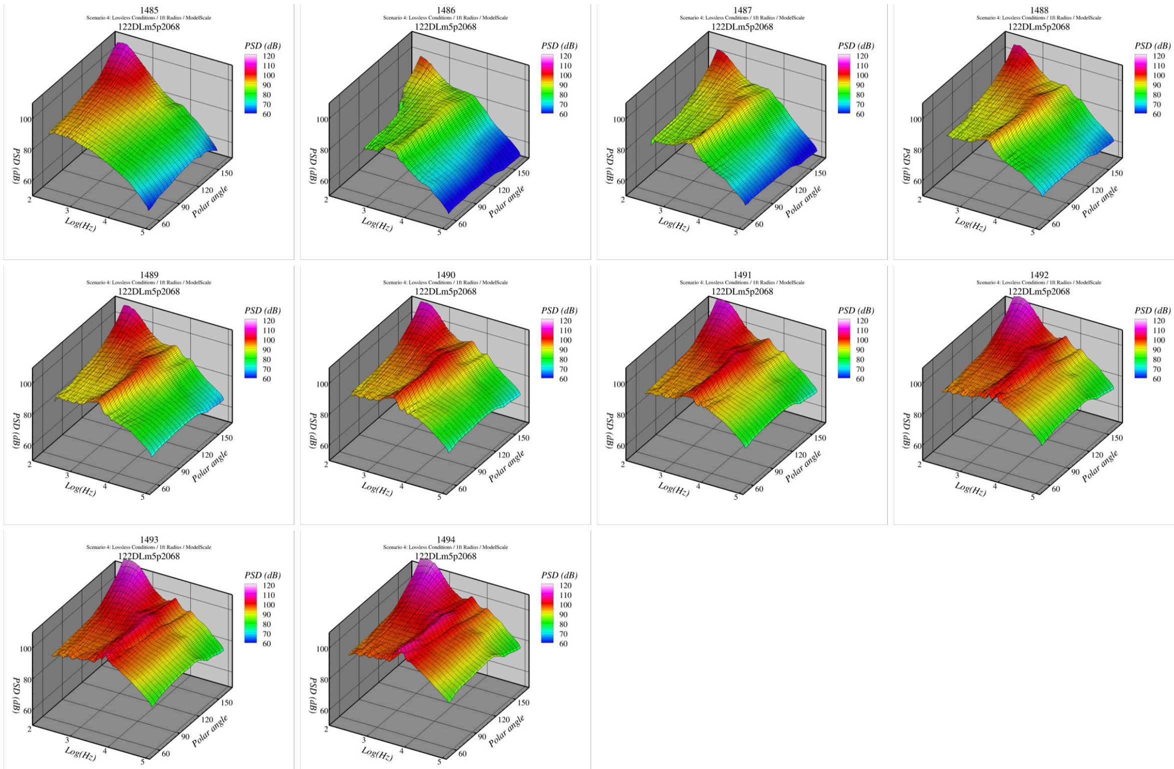

Figure 51.—Far-field PSD, 1 ft, lossless for *122DLm5p2068*, SP7+ engine matrix.

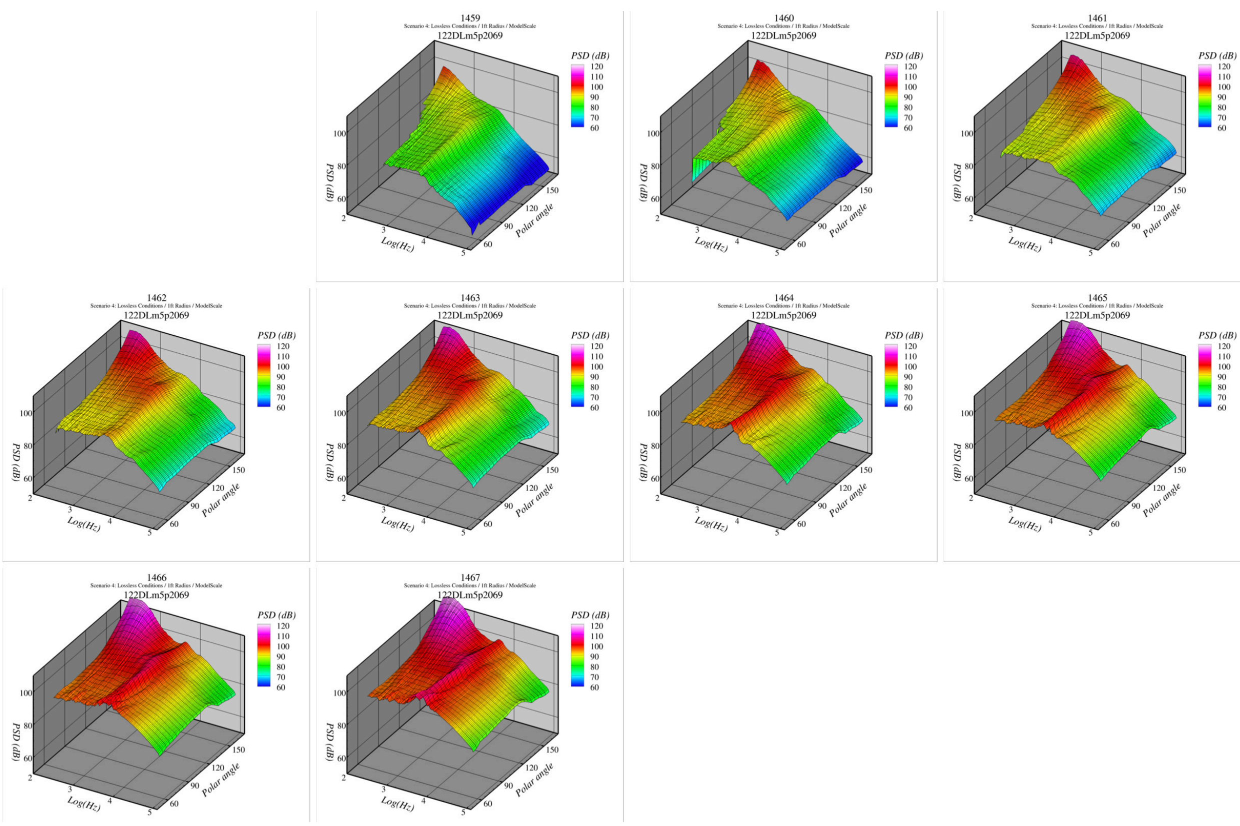

Figure 52.—Far-field PSD, 1 ft, lossless for *122DLm5p2069*, SP7+ engine matrix.

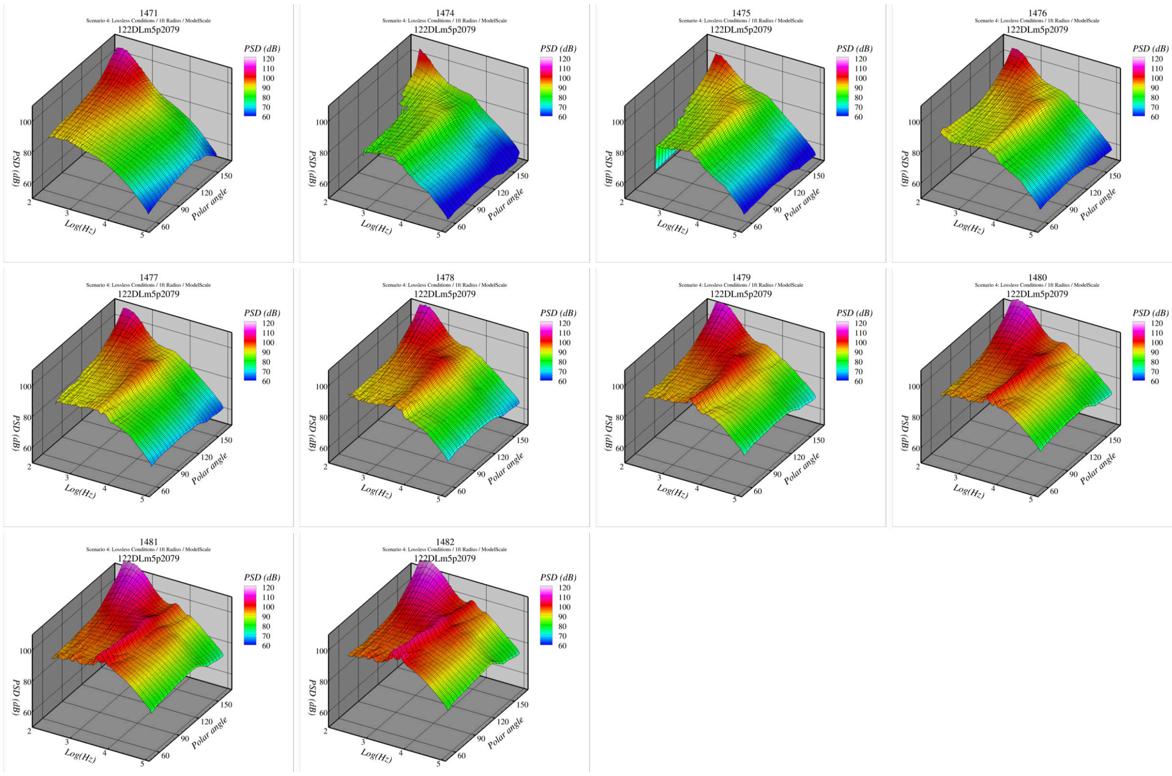

Figure 53.—Far-field PSD, 1 ft, lossless for *122DLm5p2079*, SP7+ engine matrix.

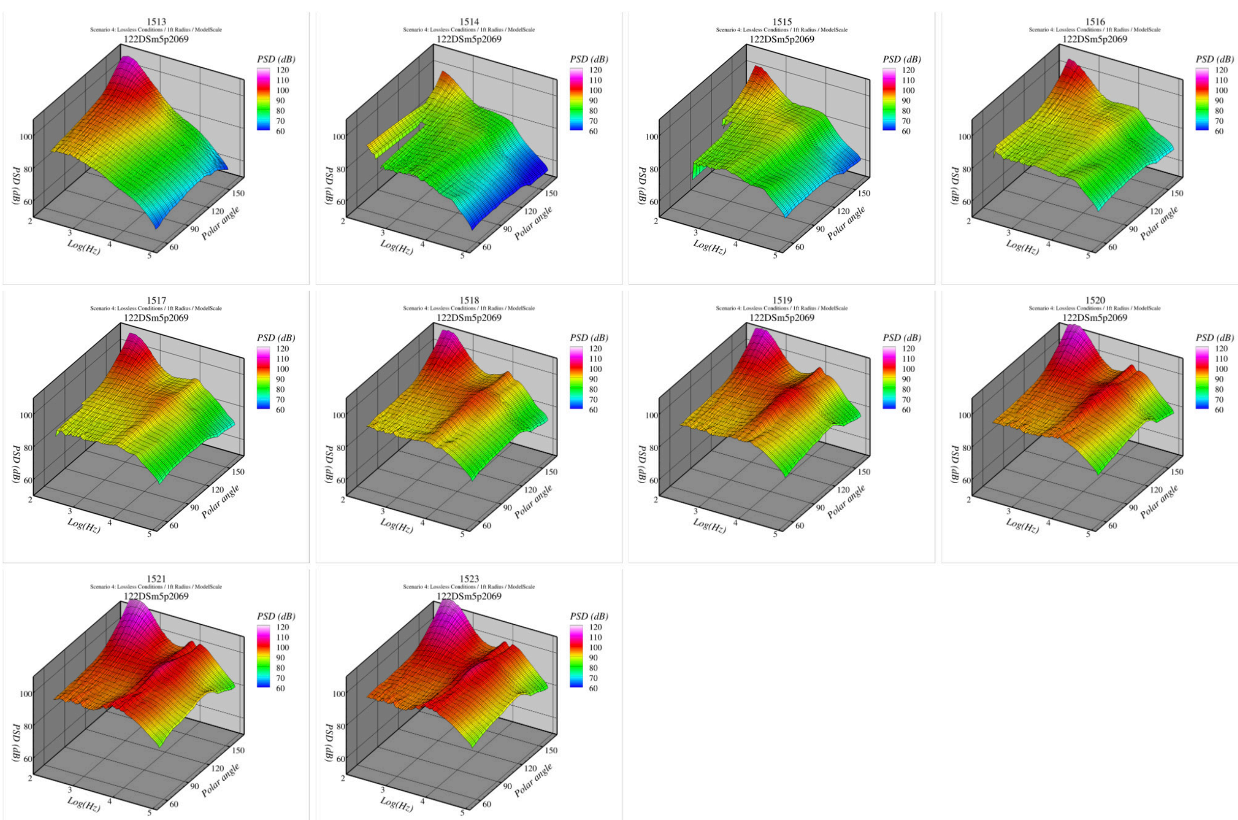

Figure 54.—Far-field PSD, 1 ft, lossless for *122DSm5p2069*, SP7+ engine matrix.

Appendices

Appendix A.—CAD Files

CAD files of nozzles tested, simplified for flow analysis. See Table 1 for listing of nozzles. Files are in STEP format, one configuration per file.

Appendix B.—Far-Field Spectral Directivities

Far-field noise measurements, in the format of spectral directivity data, are given in files, one file per configuration and setpoint. The files are ASCII with header lines describing the file and three columns of data with frequency, polar angle, and power spectral density, Pa^2/Hz in dB re 20 microPascals. After correction for microphone response and freejet refraction, the spectra have had the calculated atmospheric attenuation from nozzle exit to microphone added back and have been transformed to a 1-ft radius assuming spherical propagation from the nozzle exit.

In Appendix B, each configuration/setpoint combination has one far-field data file with the appendage '_FF.dat'. The leading part of the filename identifies the facility reading number, the configuration, and the setpoint. All the data files for a given configuration are compressed into one .zip file, identified by the configuration name (*e.g.*, *122Am0pInt_FF.zip*).

Also located in Appendix B is a tab-delimited table ('Plug20_Database.txt') listing all the data points acquired in the Plug20 test, indexed by facility reading number. Exact rig flow and ambient conditions for each data point are given in this table.

Appendix C.—BOS Measurements

The Background-Oriented Schleiren (BOS) data consists of maps of image displacement over small regions. This displacement is the result of refraction of the image integrated through the flow. The displacement has both axial and vertical components. In the data files, the displacement is in terms of image pixels. Note that the flow is from right to left in the images, just as the camera recorded the images.

In Appendix C, each configuration/setpoint combination has two data files, one for each displacement component. The axial displacement files have the appendage '_BOSx.dat', the vertical displacement files have the appendage '_BOSy.dat'. The leading part of the filenames identifies the facility reading number, the configuration, and the setpoint. All the data files for a given configuration are compressed into one .zip file, identified by the configuration name (*e.g., 122Am0pInt_BOS.zip*).

Appendix D.—Phased Array Acoustic Source Distribution Measurements

The phased array dataset consists of source distribution maps, given as .tif files with stacked images. Each image in the stack corresponds to a given frequency range, shown in the upper left corner of the image. The images also have a plot of the 1/12-octave band SPL for the center microphone in the array, and a plot of the location of the peak in the source distribution (re nozzle exit, in meters) as a function of frequency. Markers on the plots show the frequency band corresponding the source map.

In Appendix D, each configuration/setpoint combination has one .tif file with the appendage '_PA.tif'. The leading part of the filenames identifies the facility reading number, the configuration, and the setpoint. All the image files for a given configuration are compressed into one .zip file, identified by the configuration name (*e.g., 122Am0pInt_PA.zip*).

References

1. Mengle, V.G., and Dalton, W.N., “Lobed Mixer Design for Noise Suppression Vol. 1.” In NASA/CR—2002-210823/VOL1, 2002.
2. Garrison, L., Dalton, W., Lyrintzis, A., and Blaisdell, G., “On the Development of Semi-Empirical Noise Models for the Prediction of the Noise from Jets with Forced Mixers.” In 10th AIAA/CEAS Aeroacoustics Conference, American Institute of Aeronautics and Astronautics, 2004.
3. Garrison, L., Lyrintzis, A., Blaisdell, G., and Dalton, W., “Computational Fluid Dynamics Analysis of Jets with Internal Forced Mixers.” In 11th AIAA/CEAS Aeroacoustics Conference, American Institute of Aeronautics and Astronautics, 2005.
4. Chase, J., Garzon, A., and Papamoschou, D., “Directivity Effects of Shaped Plumes from Plug Nozzles.” In 51st AIAA Aerospace Sciences Meeting including the New Horizons Forum and Aerospace Exposition, American Institute of Aeronautics and Astronautics, 2013.
5. Wernet, M.P., “Real-Time Background Oriented Schlieren: Catching up with Knife Edge Schlieren.” In NASA/TM—2019-220144, 2019.
6. Wernet, M.P. “Real-Time Background Oriented Schlieren With Self-Illuminated Speckle Background.” Measurement Science and Technology, vol. 31, no. 1, 2019, p. 017001. https://doi.org/10.1088/1361-6501/ab4211.
7. Brown, C.A., and Bridges, J., “Small Hot Jet Acoustic Rig Validation.” In NASA/TM—2006-214234, 2006.
8. Cluts, J.D., Bridges, J., and Podboy, G.G. Translating Phased Array Measurements of Noise Source Locations of an Installed Jet. In AIAA SciTech Forum 2019, American Institute of Aeronautics and Astronautics, 2019.
9. Podboy, G.G., Wernet, M.P., Clem, M.M., and Fagan, A.F. Noise Source Location and Flow Field Measurements on Supersonic Jets and Implications Regarding Broadband Shock Noise. In NASA/TM—2017-219544, 2017.